Drusen, choroidal neovascularization, and retinal pigment epithelium dysfunction in SOD1-deficient mice: A model of age-related macular degeneration

Yutaka Imamura*†, Setsuko Noda‡, Kouhei Hashizume*, Kei Shinoda*§, Mineko Yamaguchi¶, Satoshi Uchiyama¶, Takahiko Shimizu¶, Yutaka Mizushima‖, Takuji Shirasawa¶, and Kazuo Tsubota*†**

*Department of Ophthalmology, Keio University School of Medicine, 35-Shinanomachi, Shinjuku-ku, Tokyo 160-8582, Japan; ‡Department of Nursing, Tokai University School of Health Science, Boseidai, Isehara, Kanagawa 259-1193, Japan; §Laboratory of Visual Physiology, National Institute of Sensory Organs, National Hospital Organization, Tokyo Medical Center, 2-5-1-Higashigaoka, Meguro-ku, Tokyo 152-8902, Japan; ¶Research Team for Molecular Biomarkers, Tokyo Metropolitan Institute of Gerontology, Itabashi-ku, Tokyo 173-0015, Japan; ‖DDS Institute, Jikei University School of Medicine, 3-25-8 Nishi-shinbashi, Minato-ku, Tokyo 105-8461, Japan; and **Department of Ophthalmology, Tokyo Dental College, 5-11-13 Sugano, Ichikawa, Chiba 272-8513, Japan

Edited by Jeremy Nathans, Johns Hopkins University School of Medicine, Baltimore, MD, and approved June 9, 2006 (received for review March 19, 2006)

Oxidative stress has long been linked to the pathogenesis of neurodegenerative diseases; however, whether it is a cause or merely a consequence of the degenerative process is still unknown. We show that mice deficient in Cu, Zn-superoxide dismutase (SOD1) have features typical of age-related macular degeneration in humans. Investigations of senescent *Sod1*$^{-/-}$ mice of different ages showed that the older animals had drusen, thickened Bruch's membrane, and choroidal neovascularization. The number of drusen increased with age, and exposure of young *Sod1*$^{-/-}$ mice to excess light induced drusen. The retinal pigment epithelial cells of *Sod1*$^{-/-}$ mice showed oxidative damage, and their β-catenin-mediated cellular integrity was disrupted, suggesting that oxidative stress may affect the junctional proteins necessary for the barrier integrity of the retinal pigment epithelium. These observations strongly suggest that oxidative stress may play a causative role in age-related retinal degeneration, and our findings provide evidence for the free radical theory of aging. In addition, these results demonstrate that the *Sod1*$^{-/-}$ mouse is a valuable animal model to study human age-related macular degeneration.

animal model | superoxide dismutase

Age-related macular degeneration (AMD) is the leading cause of legal blindness in humans in developed countries (1–5). AMD is characterized by a progressive degeneration of the macula, usually bilateral, leading to a severe decrease in vision and a central scotoma. The decrease in vision results either from retinal degeneration, called geographic atrophy (dry or nonexudative AMD), or from the secondary effects of choroidal neovascularization (CNV; wet or exudative AMD). An early sign of AMD is the appearance of drusen, which are extracellular deposits that accumulate below the retinal pigment epithelium (RPE) and are known to be risk factors for developing CNV (6–8).

Mouse models of AMD that manifest some of the features of human AMD have recently begun to appear (9–14); however, most of these mice have only some of the characteristics of human AMD (15). The severity of AMD in humans progresses with increasing age, finally resulting in extensive degeneration of the retina. Therefore, animal models that mimic the complex and progressive characteristics of AMD are needed to investigate the pathogenesis of AMD.

Oxidative stress, which refers to cellular or molecular damage caused by reactive oxygen species (ROS), has been implicated in many age-related diseases and aging itself (16, 17). ROS include free radicals, hydrogen peroxide, and singlet oxygen and are often the by-products of oxygen metabolism. The retina is particularly susceptible to oxidative stress because of its high consumption of oxygen, high concentration of polyunsaturated fatty acids, and exposure to light (18). A growing body of evidence suggests that cumulative oxidative damage may be responsible for AMD (18, 19); however, a causative link has not been definitively demonstrated (18).

To determine whether there is a causative role of oxidative stress in the pathogenesis of AMD, we first focused on the age-related changes in the eyes of mice deficient in oxidative stress scavengers. One of the main antioxidant systems in the retina is made up of three superoxide dismutase (SOD) isoenzymes that catalyze superoxide radical dismutation (20). Cu, Zn-SOD (SOD1) exists in the cytosol, Mn-SOD (SOD2) in the mitochondrial matrix, and extracellular SOD (SOD3) in the tissue interstitium as the secretory form (21). Because the amount and activity of SOD1 are highest among the three isoenzymes in the human retina (21), it seemed reasonable to hypothesize that the lack of SOD1 would accelerate age-related pathological changes in the human retina.

We have investigated the age-related changes of the retinas of *Sod1*$^{-/-}$ mice and found that these mice have many of the key elements of human AMD including drusen, thickened Bruch's membrane, and CNV. Moreover, the RPE cells of these mice show signs of oxidative damage, and their junctional integrities are damaged with the disruption of β-catenin-mediated cell adhesions. Thus, our results suggest a causative role of oxidative stress in the pathogenesis of retinal degeneration and demonstrate the critical role of SOD1 in protecting the RPE from age-related degeneration.

Results

Drusen in Senescent *Sod1*$^{-/-}$ Mice. Fundus examinations were performed on 60 *Sod1*$^{-/-}$ mice (age, 3–18 months) and 50 age-matched wild-type mice. The fundi of *Sod1*$^{-/-}$ mice ($n = 25$) under 7 months of age appeared normal and indistinguishable from those of wild-type mice ($n = 25$). Mice older than 7 months showed white to slightly yellowish retinal deposits that appeared to be similar to drusen in humans (Fig. 1*A*). The drusen were hyperfluorescent during fluorescein angiography, as in humans (Fig. 1*B*), and the numbers increased with age (Fig. 1*C*). Drusen were detected in 31 of 36 eyes (86%) of *Sod1*$^{-/-}$ mice older than 10 months. In contrast, wild-type mice and heterozygous mice

Conflict of interest statement: No conflicts declared.

This paper was submitted directly (Track II) to the PNAS office.

Freely available online through the PNAS open access option.

Abbreviations: AMD, age-related macular degeneration; CNV, choroidal neovascularization; RPE, retinal pigment epithelium; SOD, superoxide dismutase; C5, complement 5; CML, carboxymethyl lysine.

†To whom correspondence may be addressed. E-mail: imamura@sc.itc.keio.ac.jp or tsubota@sc.itc.keio.ac.jp.

www.pnas.org/cgi/doi/10.1073/pnas.0602131103

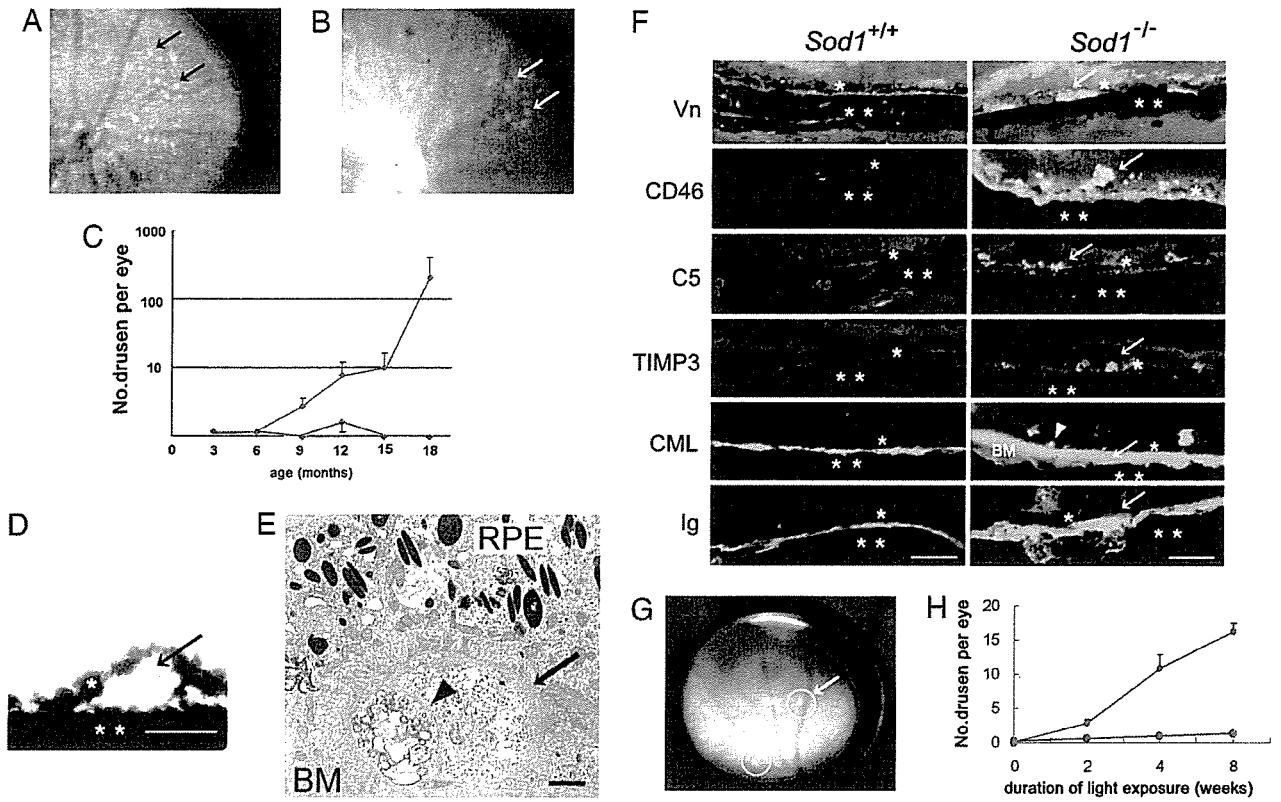

Fig. 1. Senescent *Sod1*$^{-/-}$ mice showing drusen. (*A*) Fundus photograph from a 15-month-old *Sod1*$^{-/-}$ mouse. White and slightly yellowish deposits are evident (arrows). (*B*) Fluorescein angiogram showing hyperfluorescent areas corresponding to the sites of the drusen (arrows). (*C*) Plot of the number of drusen in *Sod1*$^{-/-}$ mice at 3–18 months of age, showing an increase in the number of drusen with age. Values for *Sod1*$^{-/-}$ are plotted in red, and those for *Sod1*$^{+/+}$ are plotted in blue. (*D*) Dome-shaped deposit (arrow) between the RPE (*) and choroid (**) in a 12-month-old *Sod1*$^{-/-}$ mouse. (*E*) Electron micrograph of drusen (arrow) from a 12-month-old *Sod1*$^{-/-}$ mouse. Heterogeneous materials separated by a septum (arrowhead) are observed. The drusen appears to contain debris-like material of outer segments. BM, Bruch's membrane. (*F*) Immunohistochemistry with markers for vitronectin (Vn), CD46, C5, TIMP3, CML, and Ig. Drusen and/or their surrounding tissues from 12-month-old *Sod1*$^{-/-}$ mice (*Right*) are positive for vitronectin, CD46, C5, TIMP3, CML, and Ig in contrast to the results for age-matched wild-type mice (*Left*). *, RPE; **, choroid; arrow, positive signal; arrowhead, positive signal of CML in RPE cell layer. (*G*) Fundus changes in a 5-month-old *Sod1*$^{-/-}$ mouse after continuous light exposure for 8 weeks (white fluorescent light of 10,000 lux). Drusen are present (circles and arrows). (*H*) The number of drusen increases with the length of light exposure in *Sod1*$^{-/-}$ mice, as compared with the minimal appearance of drusen in wild-type mice. Values for *Sod1*$^{-/-}$ are plotted in red, and those for *Sod1*$^{+/+}$ are plotted in blue. (Scale bars: *D* and *F*, 50 μm; *E*, 2 μm.)

(*Sod1*$^{+/-}$) showed very few, if any, drusen (Figs. 2*A* and 3 *A*, *C*, and *E*).

Light microscopic examination of histological sections of the retinas of a 12-month-old *Sod1*$^{-/-}$ mouse showed dome-shaped deposits between the RPE and Bruch's membrane (Fig. 1*D*). Heterogeneous materials were detected beneath the RPE on Bruch's membrane by electron microscopy (Fig. 1*E*).

Markers of drusen, including vitronectin, a fluid-phase regulator binding the terminal component complex to regulate the control complex-mediated lysis (22); CD46, a membrane-bound regulator that facilitates inactivation of activated complement components (23); complement 5 (C5); tissue inhibitor of metalloproteinases 3 (TIMP3), a potent local inhibitor of matrix metalloproteinase regulating the rate of Bruch's membrane turnover (24); carboxymethyl lysine (CML); and Igs were detected in the drusen by immunohistochemistry (Fig. 1*F*).

In a proteomics analysis by Crabb *et al.* (25), vitronectin, TIMP3, and CML were found in the drusen of human cadaver eyes with AMD. In the retinas of *Sod1*$^{-/-}$ mice, positive staining for CD46, C5, and Ig was observed to extend beyond the RPE, which would indicate that the inflammatory reactions occurred, not only at the site of the drusen, but also in the surrounding tissues, including the retina (Fig. 1*F*). These findings are consistent with recent findings that local inflammation involving Igs, complements, and complement-related genes may play a role in the pathogenesis of AMD in humans (26–29).

Induction of Drusen by Exposure to Light. Because exposure to light (30, 31) and smoking (32) have been reported in epidemiological studies to be risk factors for AMD in humans, we attempted to induce drusen in young *Sod1*$^{-/-}$ mice by light exposure. Young *Sod1*$^{-/-}$ mice (age, 5 months) have normal retinal architecture and do not have any drusen. However, after constant white fluorescent light exposure (10,000 lux, equal to outdoor sunlight) for 24 h per day, drusen appeared (Fig. 1*G*), and their numbers increased with the duration of the light exposure (Fig. 1*H*)

Degeneration of RPE and Thickened Bruch's Membrane in *Sod1*$^{-/-}$ Mice. Degenerative changes of the RPE and photoreceptor cell layer are another hallmark of both the wet and dry types of AMD in humans (33). Degeneration of the RPE was observed in a 12-month-old *Sod1*$^{-/-}$ mouse by electron microscopy (Fig. 2 *A* and *B*). Bruch's membrane was markedly thickened (Fig. 2 *A* and *B*) with vacuolization of the RPE cells (Fig. 2*B*, asterisk) in a 12-month-old *Sod1*$^{-/-}$ mouse. The mean thickness of Bruch's membrane in the eyes of 10- to 12-month-old *Sod1*$^{-/-}$ mice (n = 4) was 3.2 ± 1.5 μm in contrast to that in the wild-type (n = 4, 0.5 ± 0.2 μm, $P < 0.05$). Loss of the photoreceptor cell was also

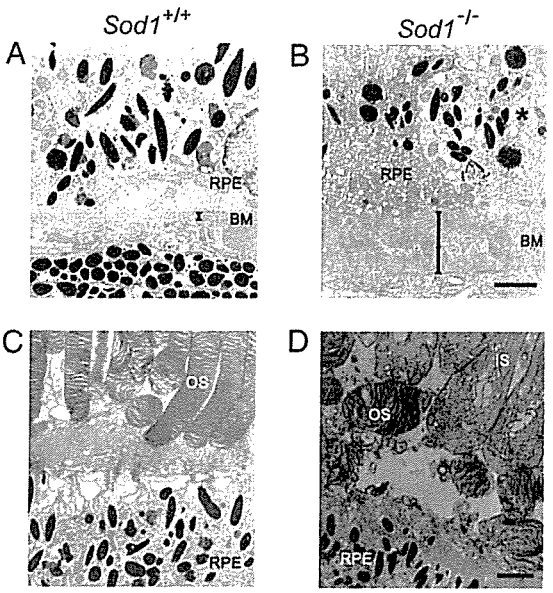

Fig. 2. Degenerated RPE and thickened Bruch's membrane in *Sod1*$^{-/-}$ mice. (*A*) Ultrastructure of Bruch's membrane (BM) in a 12-month-old wild-type mouse. (*B*) Thickened Bruch's membrane of an age-matched *Sod1*$^{-/-}$ mouse. RPE cells show marked vacuolization (*). (*C*) Ultrastructure of the outer segments (OS) of the photoreceptor cells and RPE of a 12-month-old wild-type mouse. (*D*) Destruction of inner segments (IS), outer segments, and RPE in an age-matched *Sod1*$^{-/-}$ mouse. (Scale bars: *B* and *D*, 2 μm.)

detected in 5 of 30 *Sod1*$^{-/-}$ mice (17%) that were examined histologically (representative case shown in Fig. 2 *C* and *D*). These alterations are consistent with histopathological findings in human eyes with AMD (33).

CNV in *Sod1*$^{-/-}$ Mice. The presence of CNV is a hallmark of the wet type of AMD in which the neovascularization in the choroid extends into the RPE and subretinal space. We found that 5 of 60 *Sod1*$^{-/-}$ mice (8.3%) showed an exudative lesion by fundus examination (Fig. 3 *A* and *B*), and 3 of 30 *Sod1*$^{-/-}$ mice older than 10 months (10%) had CNV by histological examination. The CNVs were confirmed by dye leakage during fluorescein angiography (Fig. 3 *C* and *D*). In contrast, the wild-type mice did not show CNV by fundus examination ($n = 50$) or histological examinations ($n = 30$).

Histological examination of the retinal sections containing the exudative lesion seen by ophthalmoscopy and area of dye leakage showed intraretinal fibrovascular tissues extending from the choroid into the retina (Fig. 3 *E* and *F*). In a 15-month-old *Sod1*$^{-/-}$ mouse, the CNV beneath the RPE can be seen to penetrate through Bruch's membrane, and the blood vessel cavity was surrounded by cells positive for CD31, a marker for endothelial cells (Fig. 3*G*). A 16-month-old senescent *Sod1*$^{-/-}$ mouse had CNV penetrating into the sensory retina (Fig. 3*H*). Electron microscopy showed ruptures of the Bruch's membrane and the RPE cell layer at the site of the CNV (Fig. 3*I*).

Oxidative Damage of RPE and Disruption of β-Catenin-Mediated Cellular Integrity of RPE in *Sod1*$^{-/-}$ Mice. Western blot analysis showed a lack of expression of SOD1 protein in the eyes of *Sod1*$^{-/-}$ mice ($n = 3$). The expressions of SOD2 and SOD3 proteins in *Sod1*$^{-/-}$ mice did not differ significantly from those in wild-type mice (Fig. 4*A*). Histochemical analysis showed the diffuse expression of SOD1 in all layers of retina of wild-type mice and the complete absence in *Sod1*$^{-/-}$ mice, in contrast to its presence in SOD2 mice (Fig. 4*B*).

A marker of oxidative damage to DNA (34), 8-hydroxy-2′-deoxyguanosine (8-OHdG), was detected in the RPE of *Sod1*$^{-/-}$ mice but was minimally present in wild-type mice (Fig. 5*A*). CML, a marker of oxidative protein modification (35), was deposited in the thickened Bruch's membrane (Fig. 1*F*) and RPE (Fig. 1*F*, arrowhead) in *Sod1*$^{-/-}$ mice, suggesting that the RPE and surrounding tissues had been damaged by oxidative processes in *Sod1*$^{-/-}$ mice.

To determine the effect of oxidative stress on the RPE, we examined whether the adherence junction proteins, which make up the barrier integrity of the RPE, were present in *Sod1*$^{-/-}$ mice (36). The location of β-catenin in the RPE of senescent *Sod1*$^{-/-}$ mice was studied in flat-mount preparations of the RPE. The presence of β-catenin was incomplete in the periphery of the RPE, indicating a disruption of the junctional integrity of the RPE (Fig. 5*B*, arrows) that is consistent with the light and electron microscopic observations (Figs. 1*D*, 2*B*, and 3 *F* and *I*). The cytoplasmic level of β-catenin was higher in the RPE cells of a 10-month-old *Sod1*$^{-/-}$ mouse than in a wild-type mouse (Fig. 5*C*). Quantitative measurement of the cytoplasmic β-catenin level of the RPE cells of 12-month-old *Sod1*$^{-/-}$ mice and age-matched wild-type mice ($n = 49$, each group) revealed a 63.3% increase in the cytoplasmic level in the *Sod1*$^{-/-}$ mice (Fig. 5*E*, $P < 0.001$). These results are compatible with an *in vitro* study showing that oxidative stress changes the cellular distribution of β-catenin and that the cytoplasmic level of β-catenin increased after the exposure of hydroxyl peroxide in ARPE-19 cells, a human RPE cell line (36).

The distribution of N-cadherin was also altered in the RPE of *Sod1*$^{-/-}$ mice (Fig. 5*D*). The expression of junction adherence proteins, including β-catenin and N-cadherin, is necessary to maintain an epithelial phenotype. Increased cytoplasmic levels of β-catenin were observed in the RPE cells of *Sod1*$^{-/-}$ mice *in vivo*, suggesting that chronic oxidative damage to the RPE may change the location of β-catenin from cell walls to cytoplasm, which then leads to the destruction of cell junctions maintained by the cadherin–catenin complex.

Because RPE damage promotes CNV growth, oxidative stress to the RPE and the disruption of β-catenin-mediated integrity may possibly be one of the initial events in this AMD model.

Discussion

Our results indicated that the retinas of senescent *Sod1*$^{-/-}$ mice have many features of the retinas of patients with AMD and recapitulated well the key elements of the human pathology. We demonstrated that drusen accumulated with increasing age in these mice, and histological examination revealed that the appearance of the drusen was quite similar to those in humans. We also showed that the major components of human drusen were present in the drusen of *Sod1*$^{-/-}$ mice and that drusen could be induced in young *Sod1*$^{-/-}$ mice by exposure to light. These findings strongly suggest that oxidative stress plays a causative role in initiating drusen formation.

Current animal models of CNV mostly use laser injury to fracture Bruch's membrane (37) or use viral transfection of angiogenic factors into RPE cells to induce CNVs (38). In our model, we used mice deficient in SOD1. The CNVs in our mice penetrated Bruch's membrane, and fluorescein angiography showed that the CNVs had a spiraling pathway into the sensory retina.

Recently, it was reported that mice deficient in *Ccl2*$^{-/-}$ or *Ccr2*$^{-/-}$ had angiogenic leakage, implying that macrophage dysfunction can induce CNV (10). These mice had retinal degeneration and drusen-like structures that increased in number with age (10). Several other mouse models of AMD have been reported. However, according to the most recent review (15), only the *Ccl2*$^{-/-}$, *Ccr2*$^{-/-}$, and *Sod1*$^{-/-}$ mice have the characteristics of both drusen and CNV. Moreover, drusen can

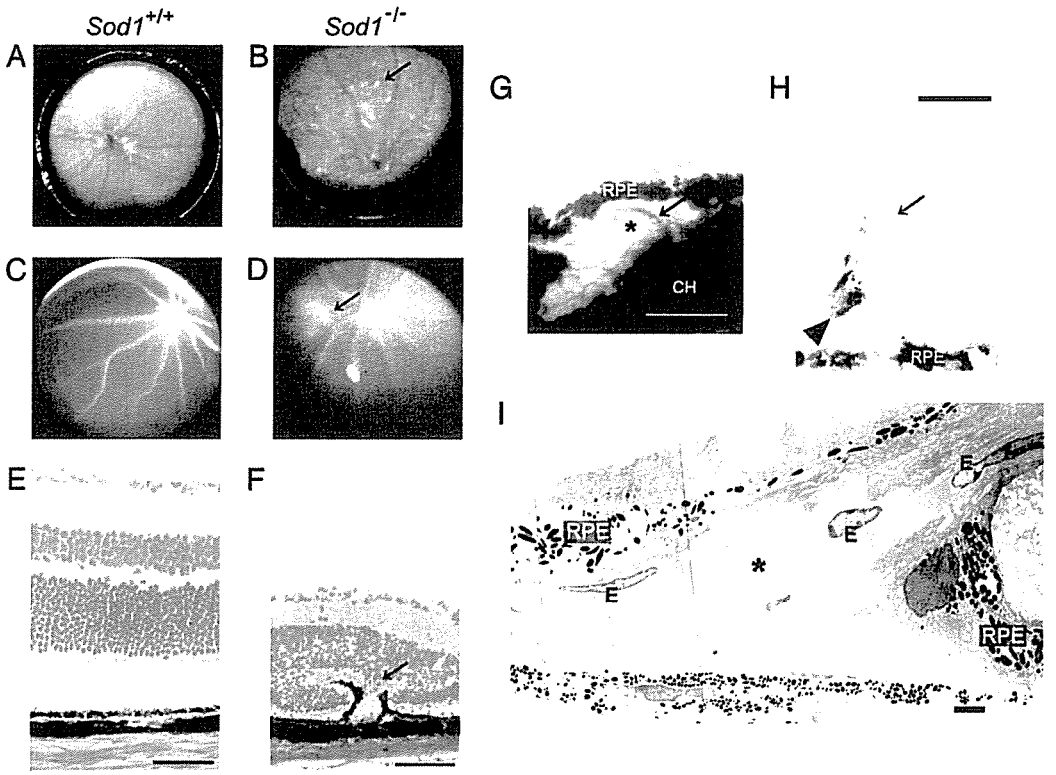

Fig. 3. CNVs in *Sod1*$^{-/-}$ mice. (*A*) Fundus of a 15-month-old wild-type mouse. (*B*) Fundus of a 15-month-old *Sod1*$^{-/-}$ mouse showing exudative retinal changes (arrow) adjacent to the optic disk. (*C*) Fluorescein angiogram of the wild-type mouse reveals no abnormal findings. (*D*) Fluorescein angiogram reveals dye leakage (arrow) from the CNV in a 15-month-old *Sod1*$^{-/-}$ mouse. (*E*) Hematoxylin and eosin staining of a retinal section of a wild-type mouse. (*F*) Fibrovascular tissue (arrow) involving RPE in the thinned retina of the *Sod1*$^{-/-}$ mouse. A thinning of the outer nuclear layer can be seen. Hematoxylin and eosin staining. (*G*) CNV in a 12-month-old *Sod1*$^{-/-}$ mouse. CNV is present beneath the RPE, and the vascular cavity (*) is surrounded by CD31-positive (diaminobenzidine) endothelial cells (arrow). Methyl green counterstaining was used. CH, choroid. (*H*) CNV with vessel cavity filled with erythrocytes (arrow) proliferates spirally into the sensory retina in a 12-month-old *Sod1*$^{-/-}$ mouse. RPE is attached within the intraretinal vascular structure (arrowhead). Toludine blue was used for staining. (*I*) Electron micrograph of CNV. CNV (*) surrounded by endothelial cells (E) pass through a defect in Bruch's membrane. RPE is severely disrupted. (Scale bars: *E–H*, 50 μm; *I*, 2 μm.)

be induced by photooxidative stress in *Sod1*$^{-/-}$ mice, which seems to be compatible with the clinical finding that subjects with a longer duration of sunlight exposure are more susceptible to soft drusen (30). Because retinal degeneration after constant light exposure was similar in the wild-type and *Sod1*$^{-/-}$ mice (data not shown), the accumulation of drusen seems to be due to the increased oxidative stress to the RPE rather than to the photoreceptors.

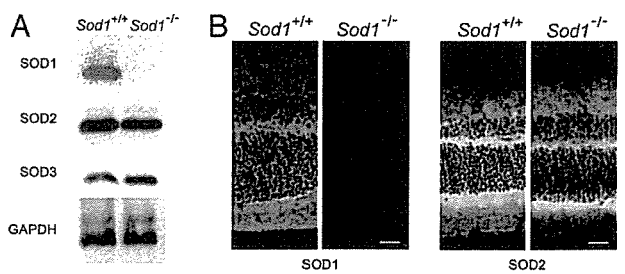

Fig. 4. Expression of SOD1, SOD2, and SOD3 in the eyes of *Sod1*$^{-/-}$ mice. (*A*) Western blot analysis reveals the absence of SOD1 protein expression in the eyes of *Sod1*$^{-/-}$ mice. The protein levels of SOD2 (Mn-SOD) and SOD3 (extracellular SOD) appear to be the same in wild-type and *Sod1*$^{-/-}$ mice. (*B*) SOD1 and SOD2 expression in the retinas of wild-type and *Sod1*$^{-/-}$ mice. (Scale bars: 50 μm.)

Our results demonstrated that complex phenotypes similar to those of human AMD can be caused by deficiency of a single gene, and the movement of β-catenin to the cytoplasm may explain the destruction of the cellular integrity of RPE. This would then contribute to the formation of drusen and CNV. Because the SOD2 and SOD3 proteins are still present in *Sod1*$^{-/-}$ mice, SOD1 as a cytoplasmic scavenger of reactive oxygen species (ROS) may play a major role in protecting RPE cells from oxidative damages.

As in other neurodegenerative disorders of the CNS, the pathogenesis of human AMD has long been linked to oxidative stress, although its causative role has not been definitively determined. Indirect evidence that oxidative damage is associated with AMD comes from epidemiological studies showing that smoking and sunlight exposure significantly increase the risk of AMD (30–32). In addition, supplementation with antioxidants including vitamin C, vitamin E, β-carotene, copper, and zinc can slow the progression of the disease (39).

SOD1 is an abundant copper- and zinc-containing protein present in the cytosol, nucleus, peroxisomes, and mitochondrial intermembrane space. Its primary function is to act as an antioxidant enzyme, lowering the steady-state concentration of superoxide (20). Therefore, our results strongly suggest that oxidative stress is not merely an associated phenomenon but a primary cause of age-related retinal degeneration.

The relationship between SOD and AMD has been studied in humans. However, the activity of SOD in erythrocytes has not

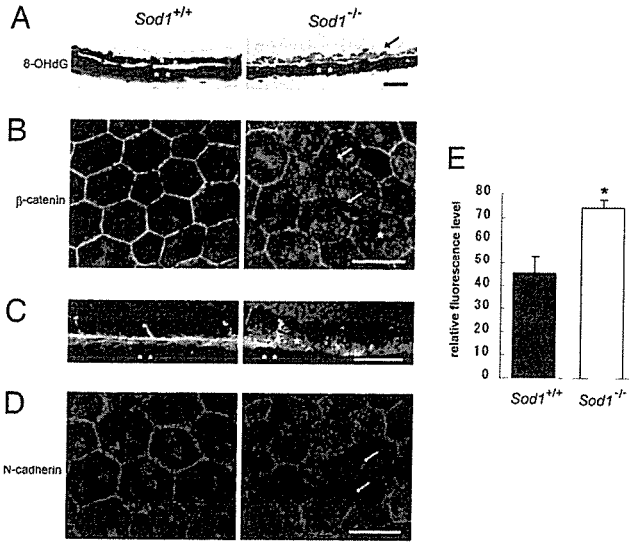

Fig. 5. Oxidatively damaged RPE and its disrupted β-catenin-mediated integrity in *Sod1*$^{-/-}$ mice. (*A*) 8-hydroxy-2′-deoxyguanosine (8-OHdG) was minimally present in the RPE of a 10-month-old wild-type mouse; however, it is markedly up-regulated in the RPE of a 10-month-old *Sod1*$^{-/-}$ mouse (arrow). *, RPE; **, choroid. (*B*) Irregular distribution of junctional proteins in RPE. β-Catenin is located at the cell walls of RPE cells in a flat-mount preparation of a 12-month-old wild-type mouse. The cytoplasmic level of β-catenin increased (*), with reduced expression at the junctional sites (arrows). (*C*) A cross-section of the RPE of a 10-month-old wild-type mouse showing staining of the cell walls by β-catenin. An absence of β-catenin in the periphery and the increasing cytoplasmic level (*) are observed in a 10-month-old *Sod1*$^{-/-}$ mouse. (*D*) Distribution of N-cadherin in a 12-month-old *Sod1*$^{-/-}$ mouse is severely disrupted, which is in contrast to the hexagonal expressions of N-cadherin in an age-matched wild-type mouse. Incomplete expression at the junctional sites can be seen (arrows). (*E*) Quantification of cytoplasmic fluorescence intensity of β-catenin in RPE cells by using the digitalized images of the flat mounts of the wild-type and the *Sod1*$^{-/-}$ mice. Randomized selected cells ($n = 49$) of each group are compared. Results are shown as mean ± SEM. *, Statistical difference between the two groups ($P < 0.001$, Student's *t* test). (Scale bars: *A*, *B*, and *D*, 50 μm; *C*, 10 μm.)

been correlated with AMD (40), and no clear relationship has yet been demonstrated in the analysis of the RPE of patients with AMD (41, 42). These studies seem not to be conclusive because the number of subjects is limited. Studies of SOD1 activity in the RPE involving larger numbers of patients are needed to determine the causative role of SOD1 in the pathogenesis of human AMD. It is also possible that some human AMD patients carry underexpressing mutations of the SOD1 gene.

Genetic polymorphism of the SOD2 gene, on the other hand, has been associated with AMD (43). Although a retinal thinning has been observed in mice deficient in SOD2, they die soon after birth and therefore are not suited for use in studies of long-term age-related retinal changes (44, 45).

In conclusion, we have demonstrated that the lack of SOD1 leads to the development of an animal recapitulating drusen, CNV, and RPE dysfunction, which could be a platform to validate therapies for age-related retinal degenerative disorders including AMD. Because β-catenin is a key molecule in constituting the integrity of the RPE cell layer, further research will be necessary to elucidate the means by which SOD1 deficiency interferes with the dynamics of β-catenin in the RPE.

Methods

Mice. *Sod1*$^{-/-}$ mice on a C57BL/6 background were generated as described (46), and wild-type C57BL/6 mice were purchased from The Jackson Laboratory. Genotyping was performed by PCR as described (46). All animal experiments were performed in accordance with the Association for Research in Vision and Ophthalmology (ARVO) Statement for the Use of Animals in Ophthalmic and Visual Research.

Fundus Photography and Angiography. Fundus examinations were performed with an indirect ophthalmoscope (Heine Optotechnik, Herrsching, Germany) and a 28-diopter lens by two masked examiners independently. Pupils were fully dilated with 0.5% tropicamide and 0.5% phenylephrine-HCL (Santen, Osaka), the fundus was photographed with a charge-coupled device (CCD) camera (CS5130; Tokyo Electronic Industry, Tokyo), and these photographs were stored as digitalized images. Angiograms were taken with a small animal fundus camera (RC2; Kowa, Tokyo, Japan), and 60 μl of 5% sodium fluorescein (Alcon Laboratories, Fort Worth, TX) per animal was injected into the tail vein.

Immunohistochemistry. The enucleated mouse eyes were immersed immediately in optimal cutting temperature (OCT) compound (Lab-Tek) and frozen in dry ice–ethanol for immunohistochemical or hematoxylin and eosin staining. For fluorescent labeling, frozen sections (8 μm) were fixed in ice-cold acetone or 4% paraformaldehyde in PBS, blocked with rabbit or goat serum, and stained with rabbit Ab to human CD46 (Santa Cruz Biotechnology) (10), rabbit Ab to C5 (Abcam, Cambridge, MA), mouse Ab to mouse CML (TransGenic, Kumamoto, Japan), rabbit Ab to human TIMP3 (Lab Vision, Fremont, CA), goat Ab to human vitronectin (Santa Cruz Biotechnology) (47), rabbit Ab to 8-hydroxy-2′-deoxyguanosine (8-OHdG) (Nikken SEIL, Shizuoka, Japan), rabbit Ab to rat SOD1 (Stressgen Biotechnologies, Victoria, Canada), and rabbit Ab to human SOD2 (Stressgen Biotechnologies). The specificity of the selected Abs to mouse tissues was confirmed by Western blot analysis (C5, TIMP3, SOD1, and SOD2). The secondary Abs were anti-Ig Alexa Fluor 488 (Molecular Probes) to goat, mouse, or rabbit. For the immunostaining of 8-OHdG, images with positive reactions were merged with images from a light microscope.

Electron Microscopy. For transmission electron microscopy (TEM), tissues were fixed in 2.5% glutaraldehyde and then postfixed in 1% OsO_4. The fixed tissues were dehydrated and embedded in Quetol 812 and sectioned with a diamond knife. Quetol 812 sections (2 μm) were counterstained with toluidine blue and examined with a light microscope. Ultrathin sections (2 μm) were stained in 2% uranyl acetate and lead citrate and examined with an electron microscope (JEM-1200EX; JEOL).

Light Exposure. Five-month-old *Sod1*$^{-/-}$ and wild-type mice were exposed to constant white fluorescent light (Toshiba Lighting and Technology, Tokyo) in a light box surrounded by mirrors (Tinker-N, Kyoto, Japan) for 24 h per day for 8 weeks. Fundus examination was performed every 2 weeks. The light intensity was 10,000 lux. Digitalized fundus images were recorded from the eyes of *Sod1*$^{-/-}$ ($n = 25$) and wild-type ($n = 25$) mice, and the number of drusen was counted by two examiners masked to the type of animal.

Western Blot Analysis. Proteins extracted from the ocular tissues of 10- to 12-month-old *Sod1*$^{-/-}$ and wild-type mice were examined by Western blot using rabbit Abs to SOD1, SOD2, SOD3 (Stressgen Biotechnologies), and GAPDH (Biogenesis, Bournemouth, U.K.).

Flat-Mount Preparations and Digital Images. The enucleated eyes from 12-month-old *Sod1*$^{-/-}$ mice and age-matched wild-type mice ($n = 4$, each group) were sectioned at the equator, and the anterior half, including the lens and vitreous, was dis-

carded. The retinas were carefully peeled from the eyecup and optic nerve by using specialized scissors and forceps under a biomicroscope (SMZ-10; Nikon). The posterior eye segment containing the sclera and choroid was dissected into quarters by four radial cuts, mounted, and air-dried. Flat mounts were examined with a fluorescence microscope (BX51; Olympus, Melville, NY). The flat mounts were stained with mouse monoclonal Ab to β-catenin (Bioscience Laboratories, Bozeman, MT) or N-cadherin (Bioscience Laboratories), preconjugated with anti-mouse Ig Alexa Fluor 488 or 594 (Molecular Probes). Fluorescein images of β-catenin were analyzed after normalization to the background, and the degree of fluorescence of the cytoplasm of each cell was calculated from average pixel intensities by using commercial software (Adobe Photoshop CS; Adobe Systems, San Jose, CA).

Statistical Analyses. All data are presented as means ± SEM, and the differences were analyzed with Student's t test. P values <0.05 were considered statistically significant.

We thank Yuka Kondo, Manabu Hirasawa, Yutaka Ohta, Ei-ichiro Nagasaka, and Masao Yoshikawa for technical assistance; Yumi Takanashi, Naoko Takayasu, and Junko Moriya for assisting with histology; Minoru Seki for angiography; Murat Dogru, Yoji Takano, Catherine Oshima, and Duco Hamasaki for reviewing the manuscript; Yasushi Inaida for financial support; and Makoto Suematsu for critical comments in interpretation of data.

1. Sommer, A., Tielsch, J. M., Katz, J., Quigley, H. A., Gottsch, J. D., Javitt, J. C., Martone, J. F., Royall, R. M., Witt, K. A. & Ezrine, S. (1991) *N. Engl. J. Med.* **325,** 1412–1417.
2. Smith, W., Assink, J., Klein, R., Mitchell, P., Klaver, C. C., Klein, B. E., Hofman, A., Jensen, S., Wang, J. J. & de Jong, P. T. (2001) *Ophthalmology* **108,** 697–704.
3. Attbo, K., Mitchell, P. & Smith, W. (1996) *Ophthalmology* **103,** 357–364.
4. VanNewkirk, M. R., Weih, L., McCarty, C. A. & Taylor, H. R. (2001) *Ophthalmology* **108,** 960–967.
5. Oshima, Y., Ishibashi, T., Murata, T., Tahara, Y., Kiyohara, Y. & Kubota, T. (2001) *Br. J. Ophthalmol.* **39,** 367–372.
6. Bird, A. C., Bressler, N. M., Bressler, S. B., Chisholm, I. H., Coscas, G., Davis, M. D., de Jong, P. T., Klaver, C. C., Klein, B. E., Klein, R., *et al.* (1995) *Surv. Ophthalmol.* **39,** 367–374.
7. Smiddy, W. E. & Fine, S. L. (1984) *Ophthalmology* **91,** 271–277.
8. Wang, J. J., Foran, S., Smith, W. & Mitchell, P. (2003) *Arch. Ophthalmol.* **121,** 658–663.
9. Hahn, P., Qian, Y., Dentchev, T., Chen, L., Beard, J., Harris, Z. L. & Dunaief, J. L. (2004) *Proc. Natl. Acad. Sci. USA* **101,** 13850–13855.
10. Ambati, J., Anand, A., Fernandez, S., Sakurai, E., Lynn, B. C., Kuziel, W. A., Rollins, B. J. & Ambati, B. K. (2003) *Nat. Med.* **11,** 1390–1397.
11. Yoshida, T., Ohno-Matsui, K., Ichinose, S., Sato, T., Iwata, N., Saido, T. C., Hisatomi, T., Mochizuki, M. & Morita, I. (2005) *J. Clin. Invest.* **115,** 2793–2800.
12. Malek, G., Johnson, L. V., Mace, B. E., Saloupis, P., Schmechel, D. E., Rickman, D. W., Toth, C. A., Sullivan, P. M. & Bowes Rickman, C. (2005) *Proc. Natl. Acad. Sci. USA* **102,** 11900–11905.
13. Rackoczy, P. E., Zhang, D., Robertson, T., Barnett, N. L., Papadimitriou, J., Constable, I. J. & Lai, C.-M. (2002) *Am. J. Pathol.* **161,** 1515–1524.
14. Weng, J., Mata, N. L., Azarian, S. M., Tzekov, R. T., Birch, D. G. & Travis, G. H. (1999) *Cell* **98,** 13–23.
15. Rakoczy, P. E., Yu, M. J. T., Nusinowitz, S., Chang, B. & Heckenlively, J. R. (2006) *Exp. Eye Res.* **82,** 741–752.
16. Andersen, J. K. (2004) *Nat. Med.* **10,** S18–S25.
17. Harman, D. (1956) *J. Gerontol.* **11,** 298–300.
18. Beatty, S., Koh, H. H., Henson, D. & Boulton, M. (2000) *Surv. Ophthalmol.* **45,** 115–134.
19. Hahn, P., Milam, A. H. & Dunaief, J. L. (2003) *Arch. Ophthalmol.* **121,** 1099–1105.
20. Valentine, J. S., Doucette, P. A. & Potter, S. Z. (2005) *Annu. Rev. Biochem.* **74,** 563–593.
21. Behndig, A., Svensson, B., Marklund, S. L. & Karlsson, K. (1998) *Invest. Ophthalmol. Vis. Sci.* **39,** 471–475.
22. Hageman, G. S., Mullins, R. F., Russell, S. R., Johnson, L. V. & Anderson, D. H. (1999) *FASEB. J.* **13,** 477–484.
23. Johnson, L. V., Leitner, W. P., Staples, M. K. & Anderson, D. H. (2001) *Exp. Eye Res.* **73,** 887–896.
24. Kamei, M. & Hollyfield, J. G. (1999) *Invest. Ophthalmol. Vis. Sci.* **40,** 2367–2375.
25. Crabb, J. W., Miyagi, M., Gu, X., Shadrach, K., West, K. A., Sakaguchi, H., Kamei, M., Hasan, A., Yan, L., Rayborm, M. E., *et al.* (2002) *Proc. Natl. Acad. Sci. USA* **99,** 14682–14687.
26. Hageman, G. S., Luthert, P. J., Victor Chong, N. H., Johnson, L. V., Anderson, D. H. & Mullins, R. F. (2001) *Prog. Retin. Eye Res.* **20,** 705–732.
27. Haines, J. L., Hauser, M. A., Schmidt, S., Scott, W. K., Olson, L. M., Gallins, P., Spencer, K. L., Kwan, S. Y., Noureddine, M., Gilbert, L. R., *et al.* (2005) *Science* **308,** 419–421.
28. Edwards, A. O., Ritter, R., III, Abel, K. J., Manning, A., Panhuysen, C. & Farrer, L. A. (2005) *Science* **308,** 421–424.
29. Klein, R. J., Zeiss, C., Chew, E. Y., Tsai, J. Y., Sackler, R. S., Haynes, C., Henning, A. K., SanGiovanni, J. P., Mane, S. M., Mayne, S. T., *et al.* (2005) *Science* **308,** 385–389.
30. Cruickshanks, K. J., Klein, R., Klein, B. E. & Nondahl, D. M. (1993) *Arch. Ophthalmol.* **115,** 514–518.
31. Wenzel, A., Grimm, C., Samardzija, M. & Reme, C. E. (2005) *Prog. Retin. Eye Res.* **24,** 275–306.
32. Vingerling, J. R., Hoffman, A., Grobbee, D. E. & de Jong, P. T. (1996) *Arch. Ophthalmol.* **114,** 1193–1196.
33. Green, R. G. & Harlan, J. B. (1999) in *Age-Related Macular Degeneration*, eds. Berger, J. W., Fine, S. L. & Maguire, M. G (Mosby, St. Louis), pp. 81–154.
34. Kasai, H., Chung, M. H., Jones, D. S., Inoue, H., Ishikawa, H., Kamiya, H., Ohtsuka, E. & Nishimura, S. (1991) *J. Toxicol. Sci.* **16,** 95–105.
35. Ishibashi, T., Murata, T., Hangai, M., Nagai, R., Horiuchi, S., Lopez, P. F., Hinton, D. R. & Ryan, S. J. (1998) *Arch. Ophthalmol.* **116,** 1629–1632.
36. Bailey, T. A., Kanuga, N., Romero, I. A., Greenwood, J., Luthert, P. J. & Cheetham, M. E. (2004) *Invest. Ophthalmol. Vis. Sci.* **45,** 675–684.
37. Semkova, I., Peters, S., Welsandt, G., Janicki, H., Jordan, J. & Schraermeyer, U. (2003) *Invest. Ophthalmol. Vis. Sci.* **44,** 5349–5354.
38. Schwesinger, C., Tee, C., Rohan, R. M., Joussen, A. M., Fernandez, A., Meyer, T. N., Poulaki, V., Ma, J. J., Redmond, T. M., Liu, S., *et al.* (2001) *Am. J. Pathol.* **158,** 1161–1172.
39. Age-Related Eye Disease Study Research Group (2001) *Arch. Ophthalmol.* **119,** 1439–1452.
40. Delcourt, C., Cristol, J. P., Leger, C. L., Descomps, B. & Papoz, L. (1999) *Ophthalmology* **106,** 215–222.
41. Liles, M. R., Newsome, D. A. & Oliver, P. D. (1991) *Arch. Ophthalmol.* **109,** 1285–1288.
42. Frank, R. N., Amin, R. H. & Puklin, J. E. (1999) *Am. J. Ophthalmol.* **127,** 694–709.
43. Kimura, K., Isashiki, Y., Sonoda, S., Kakiuchi-Matsumoto, T. & Ohba, N. (2000) *Am. J. Ophthalmol.* **130,** 769–773.
44. Li, Y., Huang, T. T., Carlson, E. J., Melov, S., Ursell, P. C., Olson, J. L., Noble, L. J., Yoshimura, M. P., Berger, C., Chen, P. H., *et al.* (1995) *Nat. Genet.* **11,** 376–381.
45. Sandbach, J. M., Coscun, P. E., Grossniklaus, H. E., Kokoszka, J. E., Newman, N. J. & Wallace, D. C. (2001) *Invest. Ophthalmol. Vis. Sci.* **42,** 2173–2178.
46. Matzuk, M. M., Dionne, L., Guo, Q., Kumar, T. R., & Lebovitz, R. M. (1998) *Endocrinology* **139,** 4008–4011.
47. Teesalu, T. T., Hinkkanen, A. E. & Vaheri, A. (2001) *Am. J. Pathol.* **159,** 2227–2237.

Clinical and Experimental Ophthalmology 2006; 34: 491–499
doi:10.1111/j.1442-9071.2006.1253.x

Letters to the Editor

Clinical Case Notes

Microcirculation at optic disc rim is correlated with visual field defects in cases of anterior ischaemic optic neuropathy

ABSTRACT

We report two cases of anterior ischaemic optic neuropathy in whom tissue blood flow at the disc rim was correlated with the visual field defect. Tissue blood flow of each eye was evaluated with Heidelberg retina flowmeter. Both cases experienced acute visual loss and an altitudinal hemianopsia associated with optic disc oedema in the affected eye. In each case, the tissue blood flow at the affected (upper or lower half) disc rim corresponding to visual field deficit was reduced compared with that at the opposite-sided half disc rim in the affected eye and with the corresponding area in the fellow eye. The reduction of blood flow in the affected half disc rim associated with the visual field defect demonstrated that retina flowmetry can detect differences in tissue blood flow between superior and inferior sectional disc rim areas as well as between eyes non-invasively.

Key words: AION, microcirculation, visual field defect

INTRODUCTION

Anterior ischaemic optic neuropathy (AION) begins with acute visual disturbances and optic disc oedema. Fluorescein angiography shows some segmental delay or optic disc staining in the area corresponding with the visual field defect. Later, the affected segment of optic disc becomes atrophic and the visual field defect is irreversible. It has been hypothesized that AION results from a disturbance of the circulation on the optic nerve head (ONH) from an occlusion of a posterior ciliary artery.[1]

The Heidelberg retina flowmeter (HRF, Heidelberg Engineering Gmbh, Heidelberg, Germany) is designed for non-invasive measurements of retinal blood flow. Reproducible and quantitative measurements of capillary blood flow are possible in distinct areas of a capillary meshwork of the eye.[2]

We present two cases of AION in which HRF demonstrated a reduction of blood flow in the optic disc rim that corresponded with the visual field defect.

METHODS

The tissue blood flow was measured five times in a $10° \times 2.5°$ area in both eyes. The areas examined were the superior and inferior disc rim and the superior and inferior paramacular areas. Each area was made up of 256 points × 64 lines, and each line was scanned 128 times. The mean blood flow (MBF) was calculated as an indicator of tissue microcirculation by the automatic full-field perfusion image analyser (AFFPIA, version 3.3, Heidelberg Engineering GmbH).[3] The ratio of the MBF between the two eyes in normal subjects is approximately 1.0.[4] The MBF was obtained by averaging three values after omitting the highest and lowest ones. The ratio of the MBF of the affected eye to the fellow eye (A/F) was calculated for each area, and the ratio of the MBF in the superior disc rim to that in the inferior disc rim (S/I) was calculated.

CASE REPORT

Case 1: A 62-year-old man noticed a sudden loss of vision in his lower visual field of the right eye. He showed an altitudinal visual field defect in the right eye by Humphrey perimetry and was referred to our unit in September 2002. He had not had any visual problems or significant family history.

On examination, he did not have a relative afferent pupillary defect, and his eye movements were normal. His best-corrected visual acuity was 6/6 in both eyes, and the intraocular pressure was 14 mmHg in both eyes. The right optic disc was swollen (Fig. 1a), but the left fundus was completely normal. Both Humphrey and Goldmann perimetry showed an inferior altitudinal hemianopsia in the right eye (Fig. 1b). Fluorescein angiography revealed a marked delayed arm-to-retina circulation time (53.3 s) in the right eye, although delayed circulation time is not typical of non-arteritic AION. The right eye was diagnosed as having AION.

The A/F ratios in each area and the S/I ratios in each eye clearly demonstrate a reduction of blood flow in the superior disc rim in the right eye (Fig. 2) which corresponded with the visual field defect (Figs 1b,2a).

Case 2: A 47-year-old man noticed a superior visual field defect after vitrectomy for vitreous haemorrhage associated with proliferative diabetic retinopathy of the right eye in Keio University hospital. The surgery was performed under retrobulbar anaesthesia and no major complication was encountered. Intraoperative panretinal photocoagulation was performed, but neither gas nor air injection was done.

On examination, the light reflex and eye movements were normal. The best-corrected visual acuity was 6/9 in the right eye and 6/6 in the left eye. The intraocular pressure ranged 14–16 mmHg without any antiglaucomatous medication. Funduscopy revealed attenuated retinal arteries and oedematous change in the inferior portion of the optic disc in the right eye (Fig. 1c). Goldmann perimetry demonstrated a superior altitudinal hemianopsia in the right eye (Fig. 1d). Fluorescein angiography showed a mildly prolonged arm-to-retina time (21.0 s) and local hyperfluorescence in the right optic disc. Visual acuity improved to 6/6 but the optic disc became pale and a visual field defect remained 6 years after surgery.

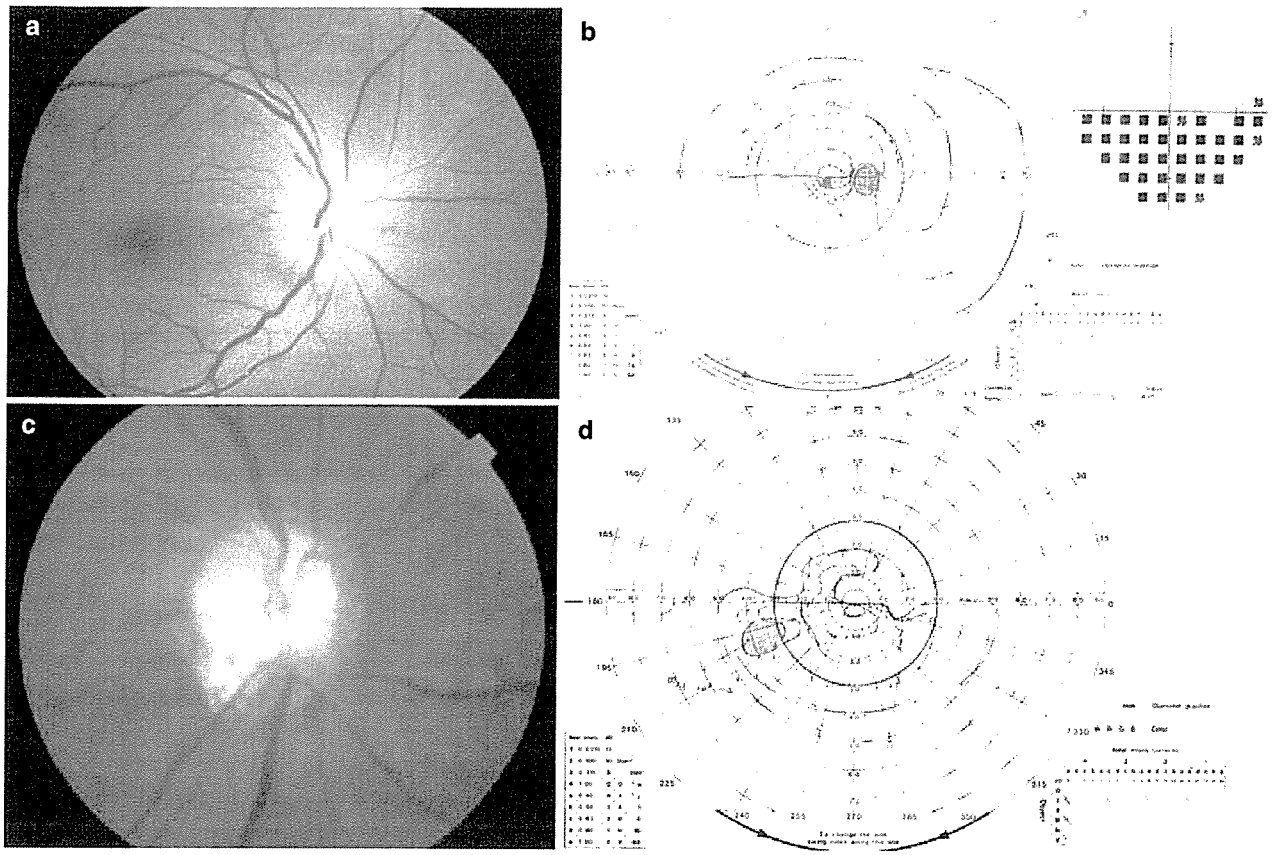

Figure 1. (a) Fundus photograph of the right eye in case 1 showing disc swelling. Sectional change is unclear. (b) Goldmann perimetry and Humphrey visual field of the right eye in case 1 showing inferior altitudinal hemianopsia. (c) Fundus photograph of the right eye in case 2 showing oedematous change in the inferior portion of the optic disc. (d) Goldmann perimetry of the right eye in case 2 showing superior altitudinal hemianopsia.

The A/F ratios in each area and the S/I ratios in each eye clearly demonstrate a reduction of blood flow in the inferior disc rim in the right eye (Fig. 2) which corresponded with the visual field defect (Figs 1d,2c).

Discussion

The main source of blood supply to the ONH is posterior ciliary artery circulation except for the surface nerve fibre layer which is supplied by the retinal circulation, and circulation pattern of the ONH has sectional distribution. It is generally believed that AION is due solely to non-perfusion or hypoperfusion of the ciliary circulation in the ONH, and not of the central retinal artery circulation in the ONH. Hayreh described that the primary objective of evaluating the ONH circulation in ischemia or vascular insufficiency of the ONH is to obtain information about the ciliary circulation in the prelaminar and deeper layers of the ONH and not the retinal circulation in the surface nerve fibre layer.[1] Flow values of disc rim obtained by HRF is considered to be a mixture of retinal and choroidal blood flow contribution because the depth of laser penetration is about 400 μm, thereby the scanning depth contains nerve fibre layer and prelaminar region. HRF measurements can be considered to be a suitable indicator closely related to the physiological status of retinal nerve fibre layer and neighbouring retinal ganglion cells. The juxtapapillary retinal blood flow was reported to be reduced in association with the structural damage of ONH in glaucoma patients by utilizing HRF.[5] The MBF measurements in our case clearly illustrated the specific circulation disturbance at the superior or inferior disc rim in the diseased eye, which corresponded with the ophthalmoscopic changes and the visual field deficit. Leiba *et al.* reported reduced microcirculation at ONH in association with altitudinal visual field defects in cases of AION by using HRF in the first place.[6] Our results reinforced their report and showed the convenience of analysis of microcirculation by using AFFPIA software.

In conclusion, our findings demonstrated that the AFFPIA for HRF instrument is a useful software for evaluating sectional ONH tissue blood flow, and can detect changes even not visible ophthalmoscopically.

Shinsuke Yokoyama MD,[1] Itaru Kimura MD,[1] Hisao Ohde MD,[1] Kei Shinoda MD[1,2] and Yukihiko Mashima MD[1]

[1]*Department of Ophthalmology, Keio University School of Medicine, and* [2]*Laboratory of Visual Physiology, National Institute of Sensory Organs, Tokyo, Japan*

Received 11 May 2005; accepted 5 December 2005.

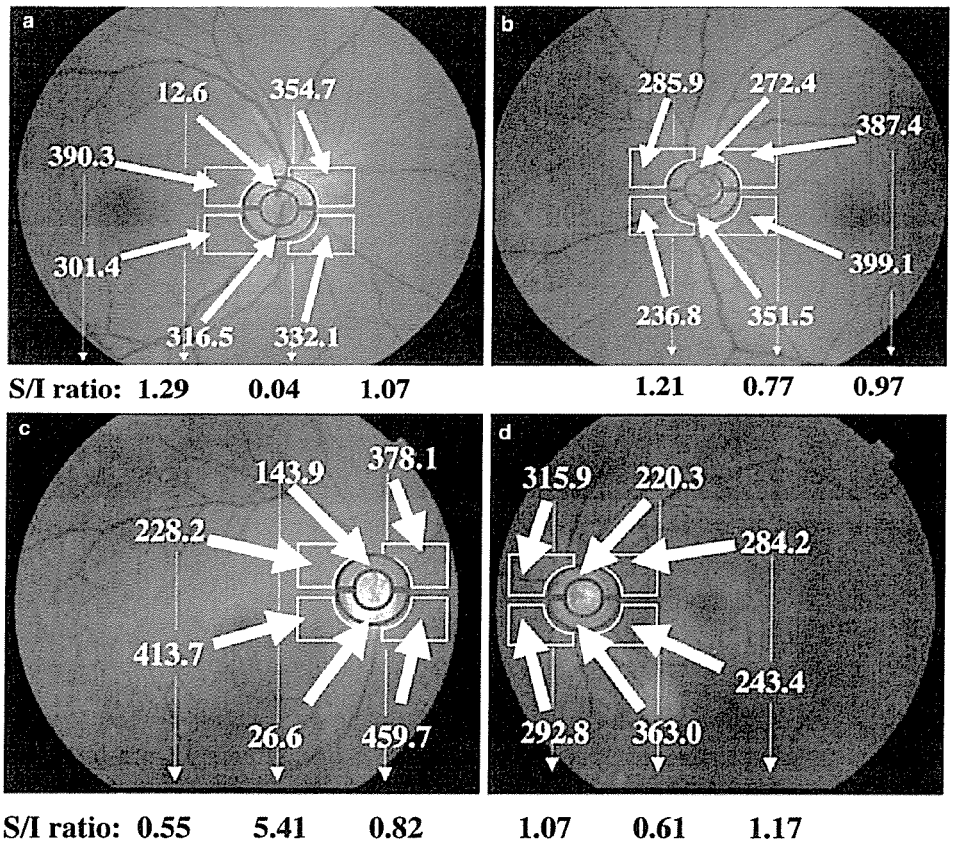

Figure 2. Mean blood flow (MBF) measurements of the disc rim and peripapillary retinal area. The area is divided into superior and inferior regions. The sectional tissue blood circulation disturbance in the superior disc rim area in the right eye was observed. MBF is indicated in arbitrary units. (a) and (b) show right and left eyes in case 1, and (c) and (d) show right and left eyes in case 2, respectively.

References

1. Hayreh SS. The blood supply of the optic nerve head and the evaluation of it – myth and reality. *Prog Retin Eye Res* 2001; 20: 563–93.
2. Michelson G, Schmauss B. Two dimensional mapping of the perfusion of the retina and optic nerve head. *Br J Ophthalmol* 1995; 79: 1126–32.
3. Michelson G, Welzenbach J, Pal I, Harazny J. Automatic full field analysis of perfusion images gained by scanning laser Doppler flowmetry. *Br J Ophthalmol* 1998; 82: 1294–300.
4. Kimura I, Shinoda K, Tanino T, Ohtake Y, Mashima Y, Oguchi Y. Scanning laser Doppler flowmeter study of retinal blood flow in macular area of healthy volunteers. *Br J Ophthalmol* 2003; 87: 1469–73.
5. Logan JF, Rankin SJ, Jackson AJ. Retinal blood flow measurements and neuroretinal rim damage in glaucoma. *Br J Ophthalmol* 2004; 88: 1049–54.
6. Leiba H, Rachmiel R, Harris A, Kagemann L, Pollack A, Zalish M. Optic nerve head blood flow measurements in non-arteritic anterior ischaemic optic neuropathy. *Eye* 2000; 14: 828–33.

Chemo-paralysis for the removal of a live intraocular worm in ocular angiostrongyliasis

Abstract

Angiostrongylus cantonensis is also called the rodent lung worm. It was first discovered in 1935 by Chen in Rattus *rattus*, in Canton, China. The rodent is the definitive host while infected mollusks, snails and crabs act as the intermediate hosts. Humans are infected by the 3rd stage larvae, either by eating undercooked intermediate hosts or by consuming vegetables.[1] It is a delicate nematode reported in Asia Pacific region most commonly in South-east Asia and has been reported from Taiwan, Thailand, Indonesia, Vietnam and Sri Lanka.[2] Anterior chamber angiostrogyliasis is extremely rare, and no previous case of ocular angiostrogyliasis from India could be found on Medline search. We report a new technique in the removal of the actively motile thread-like worm by paralysing it with intracameral preservative free lidocaine, which aids in the easy removal of the intact worm.

Key words: chemo-paralysis, ocular, angiostrongylus cantonensis

Case report

A 12-year-old boy presented with a 2-week history of diffuse pain, redness and gradual loss of vision in his left eye. He was in good health and denied any systemic complaints.

Visual Sensations during Vitrectomy

Dear Editor:

The visual sensations experienced by patients during cataract surgery have been well documented.[1–3] Here we report the visual sensations described by patients during vitrectomy under retrobulbar anesthesia. Twenty-eight men and 28 women with a mean age of 61.4±12.5 years and a variety of vitreoretinal pathologies (Table 1 [available at http://aaojournal.org]) were studied. The patients were questioned about their visual sensations during and within 3 hours after vitrectomy (Table 2 [available at http://aaojournal.org]). Fifty-four (96.4%) of the patients reported seeing lights, 46 (82.1%) reported seeing ≥1 colors, and 37 (66.1%) reported seeing movements or moving objects. Of the latter 37, 34 saw instruments, and 6 (13.0%) saw the surgeon's fingers or hands. In the 51 cases of triamcinolone-assisted vitrectomy, 24 (47.1%) reported seeing many diffuse whirling black spots. Four patients (7.1%) found the

visual experiences frightening. There was no obvious difference in the incidence of the type of sensation for the different vitreoretinal pathologies (Table 3 [available at http://aaojournal.org]). The amount of anesthesia, gender, age, and pain did not seem to affect the number of patients reporting the various visual sensations (Table 4 [available at http://aaojournal.org]). The patients who had lower amounts of anesthesia tended to experience light and color sensations more frequently, but the rates were not statistically significant. A representative patient saw colorless swirling fluid during the early phase of vitrectomy, which probably corresponded to the intraocular irrigation used during core vitrectomy. Later, he reported seeing numerous swirling black and gray spots resembling snowflakes when the white triamcinolone acetonide crystals were injected into the vitreous. Twenty-two patients described a sharply tapered shadow that moved into the center of the field just before the membranelike material was peeled off. The accuracy and precision of the descriptions was unexpected, although we have reported on a patient who not only described but also drew what he saw during vitrectomy with great accuracy.[4] These drawings illustrated how well the visual perception of the patient corresponded with the surgical procedure being performed, even when they were not focused on the retina through the optical system of the eye. The basis for the visual sensations was considered to be similar to that of other entoptic phenomena,[5] as in vitreal floaters in patients with a posterior vitreous detachment. The closer the object to the retina, the more exact will its shadow correspond to the actual shape and size of the object. This explains why some of our patients reported seeing a decrease in the thickness of the object in the center of the visual field (VF) when a rod-shaped instrument was inserted into the vitreous. In addition, patients reported only one instrument on the left side of the VF, and the shaft of the light pipe was not seen. This can be interpreted as the shadow of the instrument but not of the endoillumination probe. It is of some interest that some patients perceived blood as being red; this has been reported previously.[6] Additional investigations are needed to determine the mechanism for this phenomenon. Visual sensations are experienced by the majority of patients despite full pain control, and surgeons should warn patients of these possibilities, as they can be frightening. This should minimize the patients' anxiety and stress during surgery.

Eiko Sugisaka, MD
Kei Shinoda, MD
Susumu Ishida, MD
Yutaka Imamura, MD
Yoko Ozawa, MD
Takeshi Nakajima, MD
Hajime Shinoda, MD
Kotaro Suzuki, MD
Nanae Kawaguchi, MD
Makoto Inoue, MD
Tokyo, Japan

References

1. Au Eong KG, Low CH, Heng WJ, et al. Subjective visual experience during phacoemulsification and intraocular lens implantation under topical anesthesia. Ophthalmology 2000; 107:248–50.
2. Verma D. Subjective visual experience during phacoemulsification and intraocular lens implantation under topical anesthesia [letter]. Ophthalmology 2001;108:1004–5.
3. Rengaraj V, Radhakrishnan M, Eong KG, et al. Visual experience during phacoemulsification under topical versus retrobulbar anesthesia: results of a prospective, randomized, controlled trial. Am J Ophthalmol 2004;138:782–7.
4. Kawaguchi N, Inoue M, Sugisaka E, et al. Subjective visual sensation during vitrectomy under retrobulbar anesthesia. Am J Ophthalmol 2006;141:407–9.
5. Westheimer G. Entoptic phenomena. In: Kaufman PL, Alm A, eds. Adler's Physiology of the Eye. 10th ed. St. Louis: Mosby; 2003:441–52.
6. Mandelcorn MS, Mandelcorn E, Ananthanarayan C, Fleming IM. Some observations concerning visual perception during vitrectomy after retrobulbar anesthesia. Can J Ophthalmol 1997;32:255–6.

Available online at www.sciencedirect.com
SCIENCE DIRECT
Vision Research 46 (2006) 2675–2690
Vision Research
www.elsevier.com/locate/visres

Visual resolution with retinal implants estimated from recordings in cat visual cortex

Reinhard Eckhorn [a,*], Marcus Wilms [a], Thomas Schanze [a], Marcus Eger [a], Lutz Hesse [a,b], Ulf T. Eysel [c], Zoltán F. Kisvárday [c,1], Eberhart Zrenner [d], Florian Gekeler [d], Helmut Schwahn [d], Keisuke Shinoda [d], Helmut Sachs [e], Peter Walter [f]

[a] *Department of Physics, Neurophysics Group, Philipps-University Marburg, Germany*
[b] *Eye Clinic, Philipps-University Marburg, Germany*
[c] *Department of Neurophysiology, Medical Faculty, Ruhr-University Bochum, Germany*
[d] *University Eye Hospital, Medical Faculty, University of Tübingen, Germany*
[e] *University Eye Hospital, Medical Faculty, University of Regensburg, Germany*
[f] *University Eye Hospital, Medical Faculty, University of Aachen, Germany*

Received 14 May 2005; received in revised form 7 January 2006

Abstract

We investigated cortical responses to electrical stimulation of the retina using epi- and sub-retinal electrodes of 20–100 μm diameter. Temporal and spatial resolutions were assessed by recordings from the visual cortex with arrays of microelectrodes and optical imaging. The estimated resolutions were ~40 ms and ~1° of visual angle. This temporal resolution of 25 frames per second and spatial resolution of about 0.8 cm at about 1 m and correspondingly 8 cm at 10 m distance seems sufficient for useful object recognition and visuo-motor behavior in many in- and out-door situations of daily life.

Keywords: Retina prosthesis; Visual cortex; Spatial and temporal resolution; Electrical stimulation

1. Introduction

Retinal photoreceptors transform visual stimuli into electrical signals in normal vision. These signals are processed by intraretinal neural networks and the resulting visual information is submitted by retinal ganglion cells to subsequent visual centers. This is not so in the case of diseases of the outer retina, including macula degeneration and retinitis pigmentosa. They lead to a progressive and finally total loss of the photoreceptors. However, a large percentage of inner retinal neurons remain histologically intact (Santos et al., 1997). In particular, a large number of the retinal ganglion cells stay functionally alive and can transmit action potentials via the optic tract. Apart from the substitution of retinal function by replacing deteriorated outer retinal cells with intact sub-retinal transplants (Seiler, Aramant, & Ball, 1999), most current concepts for restituting retinal functions are based on the electrical stimulation of the remaining intact visual neurons. Electrical stimuli are meant to coarsely mimic visual inputs to subsequent visual processing.

1.1. Previous work

In recent years, two main types of retinal implants have been developed using either sub-retinal or epi-retinal

* Corresponding author. Fax: +49 6421 282 70 34.
E-mail addresses: eckhorn@staff.uni-marburg.de, reinhard.eckhorn@physik.uni-marb (R. Eckhorn).
[1] Present address: University of Debrecen, Department of Anatomy, Histology and Embryology, Hungary.

0042-6989/$ - see front matter © 2006 Elsevier Ltd. All rights reserved.
doi:10.1016/j.visres.2006.01.034

electrode arrays (e.g., Chow & Chow, 1997; Chow et al., 2001; Eckmiller, 1997; Eger, Wilms, Eckhorn, & Schanze, 2005; Humayun et al., 1996, 1999, 2003; Peyman et al., 1998; Rizzo & Wyatt, 1997; Schanze, Wilms, Eger, Hesse, & Eckhorn, 2002; Schwahn et al., 2001; Wilms, Eger, Schanze, & Eckhorn, 2003; Zrenner et al., 1997, 1999; Zrenner, 2002).

The sub-retinal devices are implanted between the pigment epithelial layer and the outer layers of the retina. Electrical stimulation with such devices directly activates the overlying retinal tissue, for example the outer plexiform layer and bipolar cells in the case of photoreceptor degeneration. The stimulation parameters can partly be determined by the electronics of the implant, and local stimulation is triggered by the light falling onto a micro-photo-diode (or—transistor) array. Stett, Barth, Weiss, Haemmerle, and Zrenner (2000) have shown in in vitro experiments in normal and degenerated rat retinae, stimulated by multi-electrode arrays, that spatial resolution at retinal level, as determined by ganglion cell recordings, is at least 70 μm corresponding to 1/3° visual angle. Chow and colleagues (2001; Chow et al. 2002) have reported implantation of a passive sub-retinal device (without external energy supply) into the eye of patients, using the method of Peyman (1998). This study was designed to examine biocompatibility of their sub-retinal devices but not their function. After a very short initial phase of diffuse phosphene perception at the site of the device no further light perception was reported by the patients. However, some improvement of still functioning retinal areas, probably due to the release of growth factors induced by the surgery, the result of subthreshold electrical stimulation or the presence of the device itself, have been reported by some of the patients.

Epi-retinal implants are placed from the vitreous side onto the ganglion cell and nerve fiber layer of the retina. In response to visual stimulation through an external image sensor-array, combined with a real-time retina-processor (e.g., see Eckmiller, 1997), the epi-retinal implant evokes action potentials in retinal ganglion cells and their fibers. Finally, both types of implants send visual information in the form of spike patterns of the ganglion cells via the optic nerve to central visual structures.

In recent experiments, the retina of blind patients was electrically stimulated and they reported sensations of light spots in response to focal electrical stimulation of the inner retina (Humayun et al., 1996, 1999, 2003; Rizzo & Wyatt, 1997). These experiments clearly demonstrated the feasibility of generating perception of light patterns in blind people by retinal stimulation. Presently, no final conclusion can be drawn from the first experiments with patients about how close retinal implants meet the below given estimates of minimal requirements for useful artificial vision.

Some principal technical and biophysical problems have been solved for visual prostheses in recent years (Chow & Chow, 1997; Eckmiller, 1997; Hesse, Schanze, Wilms, & Eger, 2000; Humayun, Probst, Juan, McCormick, & Hickingbotham, 1994; Humayun et al., 1996, 1999, 2003; Normann, Maynard, Guillory, & Warren, 1996; Normann, Maynard, Rousche, & Warren, 1999; Rizzo et al., 1999; Schanze et al., 2002; Stett et al., 2000; Wilms et al., 2003; Wyatt & Rizzo, 1996; Zrenner et al., 1997, 1999; Zrenner, 2002). However, one crucial question remains regarding the type of neural responses evoked in the visual cortex by stimulation with retinal implants. To be potentially useful for visual perception, spatial, temporal, and intensity resolutions must be sufficient to discriminate objects in a static environment and to perceive motion in the dynamic scenes of everyday life.

1.2. Minimal requirements for useful artificial vision

Object recognition relies mainly on spatial resolution. A resolution better than 0.5° of visual angle corresponds to a visual acuity of 1/35 where clinically vision testing starts. 0.5° visual angle is therefore the ultimate goal in the development of retina implants. 2° resolution will lead to *improvement of performance in daily life*, like the recognition of objects that are important for taking meals, for washing, and dressing. Finally, 10° resolution might be sufficient for *mobility and orientation*, allowing subjects to perceive the presence of large objects and their movement directions (e.g., Legge, Ahn, Klitz, & Luebker, 1997). However, gaining at least some improvement of performance in daily life would be highly valuable for blind people and even regaining some mobility and orientation could improve their quality of life considerably. In normal visual processing, spatial resolution can be estimated at any stage of the visual system from the size of the classical receptive fields (CRFs) of its neurons. Inversely, spatial resolution can also be estimated from the spread of neural activation in the primary visual cortex in response to focal retinal stimulation as is done with small visual stimuli and electrical impulses in this investigation.

Minimal requirements for useful artificial vision can be estimated by psychophysical methods (e.g., Cha, Horch, & Normann, 1992a; Legge et al., 1997; Sommerhalder et al., 2003). Near perfect reading at central retinal projection sites requires at least 300 sampling points of the text to be read within about 5° retinal eccentricity. If safe navigation in dynamic out-door environments is also required, stimulation should include eccentricities of 10–15° (Cha et al., 1992a; Geruschat, Turano, & Stahl, 1998) where spatial resolution for navigational purposes can be lower. About 200 additional sampling points are sufficient within this outer "navigational belt." The number of required sampling points and their spatial distance define the required number and spacing of stimulation electrodes in a retinal implant. With the above psychophysical estimates, a total of about 500 electrodes would be necessary for useful artificial vision.

1.3. Intensity and time resolution

Retinal ganglion cells transmit retinal visual information to higher visual centers—in normal vision and with retinal

implants (independent of epi- or sub-retinal stimulation). Single ganglion cells code, to a first approximation, temporal sequences of local contrasts (intensities) within their receptive fields by spike rate modulations, based on the synaptic preprocessing in the network of inner and outer retinal neurons. This means that the coding resolutions of intensity/contrast and time are intimately related. As the maximal spike rate of a ganglion cell is limited, the number of different successive intensity values that can be transmitted in the absence of noise in terms of Shannon information (Eckhorn & Pöpel, 1975, 1981; Eckhorn, Grüsser, Kröller, Pellnitz, & Pöpel, 1976; Eger et al., 2005; Rieke, Warland, de Ruyter van Steveninck, & Bialek, 1998; Shannon, 1948) is mainly determined by the amount of time available for transmitting a single contrast value. For example, if a neuron can discharge maximally 32 action potentials during 333 ms (average duration of ocular fixation) it can theoretically code one out of 32 different intensity values within each of the 3 fixation intervals per second (or 5 bit of information in 333 ms which equals 15 bit/s). This resolution seems sufficient for most visual fixation tasks in which spatial details and high resolution of contrasts play a prominent role. If, on the other hand, a pedestrian wants to cross a road in heavy traffic, local contrast resolution is of minor importance, and may be reduced to only 4 different values (resembling 2 bit). However, in such a situation temporal resolution is of vital importance, and needs to be markedly increased to enable effective coding. Our example neuron can at best signal 2 bit by 1–4 spikes per time window of 41.7 ms. Hence, within one second it can transmit 24 times 2 bit equal to 48 bit/s (again assuming the absence of noise). This example demonstrates that a reduction in intensity resolution (from 5 bit to 2 bit per sample or frame) results in a concomitant increase of temporal resolution (from 3 to 24 samples per second) and an overall increase in the rate of information from 15 bit/s to 48 bit/s. It is important to keep in mind that the signals carrying the information are in first approximation spike densities (rates) that can be read out by the succeeding stages of the visual system at quite different speeds (integration window) with the consequence that an increase in temporal resolution reduces the contrast resolution while overall rates of information can increase. It is probable that the visual centers adaptively change the temporal resolution (Agmon-Snir & Segev, 1993) according to the current visual situation which, in turn, affects the available contrast resolution. Retina implants have to generate spike density coding so that the visual centers can use their flexible strategy in which the trade-off between intensity and time resolution is continuously optimized.

1.4. Estimates of spatial and temporal resolutions from anesthetized cats

Before extensive investigations of perceptual resolution with retina implants are carried out in blind humans, we considered it ethically appropriate to test and optimize stimulation with retinal implants in animal models. Based on the existing broad knowledge about the visual systems of cats (e.g., Gilbert, 1993; Hubel & Wiesel, 1962; Tusa, Palmer, & Rosenquist, 1978; overview: Orban, 1984), we used this species to estimate the achievable resolution in human visual perception with sub- and epi-retinal implants. Most importantly, for identical visual stimuli, human visual perception has been shown to correlate with the receptive field properties of visual cortical neurons in lightly anaesthetized monkeys and cats. Correlations were demonstrated for a variety of perceptual and neural thresholds of visual cortical neurons, including those for luminance and color contrast, flicker frequency, movement direction, and velocity (e.g., Gilbert & Wiesel, 1990; Grind van de, Grüsser, & Lunkenheimer, 1973; Heydt von der & Peterhans, 1989; Knierim & van Essen, 1992; Salzman, Britten, & Newsome, 1990; Wachtler, Sejnowski, & Albright, 2003; overview: Tovee, 1996). From these observations and retinal lesion experiments in primary visual cortex, one can conclude that perception of visual details requires the activation of neurons in this area (e.g., Darian-Smith & Gilbert, 1995). From the time course of their activations by a focal retinal stimulus impulse estimates of perceptual temporal resolution should be possible (Dinse & Krüger, 1994; Grüsser & Creutzfeld, 1957; Rager & Singer, 1998; review in: Bullier, Hupe, James, & Girard, 2001). In addition, the spatial extent of the cortical activations to such stimuli can give conservative estimates of spatial visual resolution. This is possible because the lower visual cortical areas (particularly area 17/V1) are retinotopically well organized so that spatial profiles of cortical activations can directly be related to retinal and visual space (Adams & Horton, 2003; Angelucci, Levitt, Walton, Hupé, & Bullier, 2002; Tusa et al., 1978). These measures were verified in our investigation by light stimulation of the retina before implantation of electrodes combined with recordings of cortical activities from the identical positions used during electrical stimulation.

2. Methods

Stimulation experiments with cortical electrode recordings were performed in 9 adult cats in 13 sessions, and with optical cortical recordings in 4 adult cats (3–5 kg). All experiments were done in accordance to the guidelines of the European Communities Council Directive (86/609/EEC) and were approved by official German Animal Care and Use Committees following the NIH Principles of Laboratory Animal Care (Publication 86–23, revised 1985) and the ARVO guidelines.

2.1. Preparations

Preparations for cortical microelectrode and optical recordings were similar as reported in detail elsewhere (Kisvarday, Buzas, & Eysel, 2001; Schanze et al., 2002; Wilms et al., 2003). Briefly, adult cats received an initial anesthesia with ketamine hydrochloride (Ketanest, 10 mg/kg) and xylazine hydrochloride (Rompun, 1 mg/kg) that was about 2 h later maintained by a mixture of N_2O/O_2 (70%/30%) and halothane (0.3–0.8%, optical imaging experiments) or isofluorane (0.5–1.5%, microelectrode recording experiments) using oro-tracheal intubation for artificial respiration. Eye movements were minimized by i.v. infusion of alcuronium chloride (0.1 mg/(kg h)). End-tidal CO_2 (3–4%), blood pressure (100–140 mmHg), and body temperature (38–39 °C) were monitored continuously.

Semi-chronic preparations for cortical microelectrode recordings were made with initial surgery and anesthesia (induced and prolonged) corresponding to the acute preparations except for the use of oro-tracheal intubation instead of tracheal cannulation for artificial ventilation. For head fixation and the attachment of a recording chamber over the craniotomy at V1/V2 positions, two bolts were implanted in cavities of the forehead. In some cases, an optically controlled laser coagulation of the peripheral retina was performed to reduce the risk of a retinal detachment due to vitreal tractions after insertion of stimulation electrodes.

The refraction of the non-implanted eye was corrected for the viewing distance of the visual stimulation screen at 1.3 m in front of the eyes.

2.2. Insertion of electrodes for epi-retinal stimulation

After lateral canthotomy at one eye the conjunctiva was incised (~1 mm), and a sclerostomy performed behind the limbus, sufficient for insertion of the epi-retinal fibre-microelectrode stimulation arrays. Alternatively, epi-retinal foil electrode arrays (polyimide–platinum thin-film electrodes) were implanted after lensectomy and vitrectomy through corneal incisions and placed on the retinal surface adjacent to the fovea centralis. The position of the foil electrode array was stabilized with Perfluordecalin.

Insertion of fiber- and thin-film electrodes for epi-retinal stimulation was made as described in detail by Schanze et al. (2002). Briefly, the fiber electrodes (80 μm shaft diameter; Reitböck, 1983) were ground to expose a metal (PtW) cone tip (~20 μm diameter, ~30 μm height) allowing safe charge delivery of up to 20 nC per impulse. The fiber electrodes were axially positioned singly under visual control using a computer driven, adapted fiber electrode manipulator (Eckhorn & Thomas, 1993; 1 mm concentric bundle of 3 or 7 electrode guide tubes) attached to another specially developed manipulator with 11 degrees of freedom (NeuroPhysics, University of Marburg). This system allowed fast, precise, and flexible electrode positioning through the small scleral opening (1.1 mm). In several experiments (see Section 3), thin-film arrays (platinum islands of 100 μm diameter on polyimide) were used for stimulation (Stieglitz, Beutel, Schuettler, & Meyer, 2000). For low energy activation, the electrodes were brought in direct contact with the inner limiting membrane under visual guidance. To control correct positioning, multiple unit activity (MUA) of retinal ganglion cell fibers was recorded via the stimulation electrodes.

2.3. Insertion of electrodes for sub-retinal stimulation

For a safe introduction of sub-retinal implants, the approach with access through the vitreous body of the eye (ab interno) as published by Peyman et al. (1998) as well as Sachs et al. (1999) was used. In short, a modified pars-plana-vitrectomy approach was used in the eyes after pupil dilation with atropine 1%. The high reflectivity of the tapetum lucidum required no endoillumination, thereby enabling two port vitrectomy. Two sclerotomies were made 6.0 mm posterior to the limbus. After partial vitrectomy between sclerotomy and area centralis, a 31 gauge cannula (Visitec, Sarasota, FL) was used to create a localized retinal bleb by injecting a small amount of balanced salt solution; the bleb was enlarged by injecting Healon® (Pharmacia, Stockholm, Sweden). A 2.5-mm retinotomy was then made circumferentially at the temporal portion on the bleb. The foil was introduced into the vitreous cavity with an intravitreal end-gripping forceps. After the foil was inserted through the retinotomy into the sub-retinal space, it was forwarded about 1 mm outside the created bleb under the retina near the area centralis (Volker et al., 2006).

The stimulation array consisted of thin-film platinum electrodes mounted on a flexible polyimide foil (Fraunhofer Instit. Biomed. Engin., St. Ingbert, Germany; model RS8-50; Stieglitz et al., 2000). The flexible foil strip was made of 50 μm thin polyimide with 8 substrate-integrated, insulated golden connection lanes terminating in a 2 by 4 array at the end of the strip with an even spacing of 330 μm (see Fig. 4). Rectangular openings (100 μm × 100 μm) in the insulation layer at the terminals of the lanes define the size of the stimulation electrodes. The gold electrodes were covered with a thin layer of platinum to enhance the safe charge injection capacity. At the other end of the foil strip a plug was soldered to the contact pads to allow connection with the computer controlled stimulator device (STG 1008, Multi Channel Systems, Reutlingen, Germany). At the end of each experimental session, sclera and conjunctiva were sutured, all wounds topically medicated, and infections were prevented by injections of penicillin (i.m.). The animals recovered rapidly so that after a few weeks repetitive investigations of the same eye could be performed (Gekeler et al., 2004).

2.4. Stimulation and recording

2.4.1. Epi- and sub-retinal stimulation

For epi-retinal stimulation generally rectangular constant current impulses were applied (~200–250 μs duration per polarity; ±1–150 μA). They consisted of charge balanced pairs of a negative and positive phase (cathodic first; controlled constant current sources developed by T. Schanze, manufactured by M. Eger, Uni-Marburg, Physics Department). In some cases, bursts of 2–10 such impulse-pairs were applied (0.4–2.0 ms burst duration). In optical imaging experiments, trains of biphasic stimuli were also applied (see below). For sub-retinal stimulation (see, e.g., Fig. 1B) biphasic impulses (anodic first) with amplitudes up to ±50 μA were applied against a ground electrode. Stimulus duration was 0.5–1.0 ms per phase applied at intervals of ISI = 305 ms.

Before optical imaging the visual cortex, the function of the retinal implant was tested by electrode recordings from the optic tract, made with a concentric bipolar tungsten electrode (SNEX-100, Rhodes Medical, Woodland Hills, CA, USA). Penetrations were performed at Horsley–Clarke coordinates A14/L2 just behind the optic chiasm. For positioning of the recording electrode at the correct depth, recordings were made during 1 Hz stroboscopic light flash stimulation. The optimal position of the electrode was reached, when the maximal flash evoked field potentials were obtained and the electrode was fixed at this position using dental cement. To compare the visual response amplitude to the electrically evoked responses and to judge the relative efficacy of stimulation at the different electrodes in the epi-retinal array, short, single biphasic electrical stimuli (4–78 μA; balanced current; waveform: 250 μs negative; 250 μs off; 250 μs positive) were delivered at 1 Hz via all single electrodes of the implant against ground (electrode No. 19, see Fig. 4A).

With sub-retinal stimulation, optic tract responses were evoked by electrical stimulation (±50 μA, biphasic current pulses as described above). Electrodes 1, 2, 3, and 4, respectively, served as different electrodes, the combined electrodes 5–8 of the implant were used as ground. The small field potentials were averaged from 128 repetitive stimuli (see Fig. 4B).

Cortical electrode recordings were made in area 17 and 18 (Horsley–Clarke coordinates: A2-P7, L0.5-L3) with up to 16 microelectrodes. For technical details, see Wilms et al. (2003). Briefly, linear arrays of fiber electrodes (2–3 M at 1 kHz) were used and signals were extracted in real time from each electrode's broad band recording: single unit spike activity (SUA), multiple unit spike activity (MUA), and local field potentials (LFP, 1 or 10–140 Hz). SUA was captured as events whereas the continuous amplitude signals MUA and LFP were sampled at 500 Hz. Alternatively, the broad band raw signals (1–4000 Hz) were sampled at 20 kHz for off-line filtering to SUA, MUA, and LFP, enabling a better rejection of the stimulation artifacts (Schanze et al., 2002). All signals were stored on a hard disk for off-line data evaluations.

2.5. Receptive fields

The receptive fields (RF) of the recorded cortical neurons were determined qualitatively using a hand held projector and quantitatively with computer generated stimuli presented on a monitor (100 Hz frame rate, high contrast), composed of random m-sequences (multifocal RF-measurements, Sutter, 2001). After simultaneous on-line mapping of all cortical RFs, the positions of the retinal RFs were determined by the same MUA recording method. The tip positions of the stimulation electrodes and retinal landmarks (blind spot and area centralis) were marked by rear projection onto a tangent screen using a custom designed laser projection

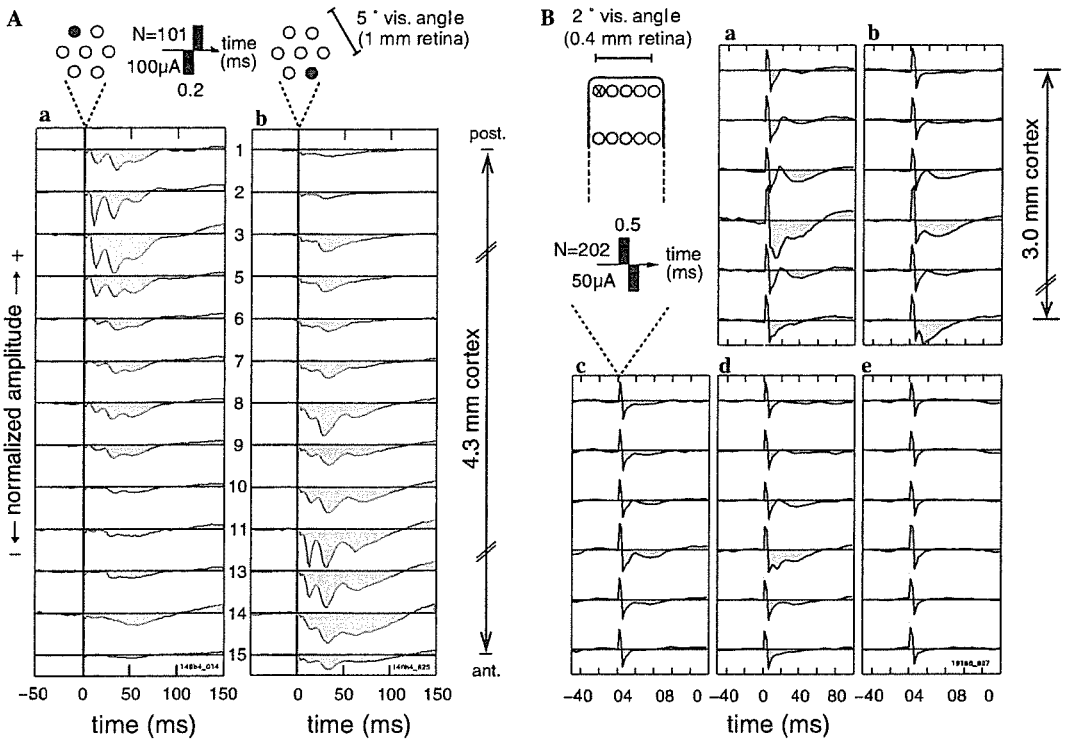

Fig. 1. Time courses of cortical population activities (LFP) in response to single-site retinal stimulation. (A) Responses to epi-retinal impulse stimulation ($N = 101$ identical stimulus repetitions) recorded simultaneously at 13 different locations by a linear electrode array (0.3 mm equi-distant pitch). The 10 ms gray band marks the primary cortical signals in direct response to the afferent stimulus evoked population spike. (B) Responses to sub-retinal impulse stimulation ($N = 202$) at five retinal electrode positions (a–e) recorded simultaneously at six different cortical locations by a linear electrode array (0.5 mm equi-distant pitch). The insets on top of column (A) and (B) depict the geometry of retinal stimulation sites and the time courses of stimulation current impulses with durations of 0.2 ms (A) and 0.5 ms (B). The retinotopic correspondence between retinal stimulation and cortical recording sites can be derived from the responses. The higher the response amplitudes the better the correspondence. This means for (Aa): best correspondence with electrode 3. For (B) the stimulation electrodes, used for the data in (Ba–e), are marked by gray background. Correspondence: electrodes used for (Ba) and (Bb): upper row left and right, respectively; for (Bc): lower row left and for (Be): lower row gray field right. Best retinotopic correspondence for data in (Ba and c–e) with electrode 4 (counted from top of each panel), for data in (Bb): el. 4 and 6.

system. Retinal electrode positions were corrected until cortical and retinal RFs sufficiently overlapped.

2.6. Optical imaging of intrinsic signals

Optical imaging of intrinsic signals was carried out using the Imager 2001 and the data acquisition software VDAQ-NT (both Optical Imaging, Germantown, NY, USA) as reported previously (Kisvarday et al., 2001). Briefly, a bilateral craniotomy was made between Horsley–Clarke coordinates AP −6 and +12 and LM +0.5 and +7 to expose the central visual representation of visual areas 17 and 18. A round stainless steel chamber (31 mm diameter) was mounted over the exposed cortical region, the dura-mater was removed and the chamber filled with silicone oil (50 cSt viscosity, Aldrich, Milwaukee, WI, USA) and sealed with a round cover-glass. During data acquisition, the camera (two SMC Pentax lenses, 1:1.2, $f = 50$ mm, arranged in a "tandem" manner, Ratzlaff & Grinvald, 1991) was focused 650–750 µm below the cortical surface and the cortex was illuminated with 609 ± 5 nm light (filter: Omega Optical, Brattleboro, VT). Imaging was carried out separately for visual stimuli through the non-operated control eye and for electrical activation via the implanted retinal electrodes.

2.6.1. Optical imaging using visual stimulation

Visuotopic mapping was performed using test stimuli presented on a video screen (SONY, Pencoed, UK) in 120 Hz non-interlaced mode 28.5 cm in front of the cats' eyes using the VSG Series 3 stimulus generator system (Cambridge Research Systems, Rochester, UK). The test stimulus consisted of a narrow horizontal slit (0.5–3 deg width and 40 deg length) encompassing a high-contrast vertical grating (50% duty cycle) 0.6–1 cyc/deg spatial frequency moving forth and back at 1–2 Hz. Stimuli were presented at visual field elevations encompassing the central 10 degrees and displayed in a random sequence. Each data acquisition period (4.5 s during which the stimulus grating moved) was preceded by an inter-stimulus interval of 10 s when the animals viewed a blank screen (average luminance of the stimulus grating).

2.6.2. Optical imaging using electrical stimuli

For obtaining intrinsic signal images of cortical activation due to electrical stimuli of the implanted electrodes a data acquisition paradigm similar to that of the visual stimulation was used (4.5 s duration, 10 s inter-stimulus interval). During a single data acquisition period, 9 trains of current pulses were applied (250 ms train duration with 250 ms intervals). Each train consisted of a barrage of 0.75 ms bipolar current pulses (±4–78 µA, 250 µs negative, 250 µs baseline, 250 µs positive repeated at 100 Hz).

2.6.3. Analysis of the optical images

For data analysis, single condition maps (SCMs, c.f. Bonhoeffer & Grinvald, 1996) were calculated by summing the images associated to a particular stimulus condition using the Winmix software (Optical Imaging, Germantown, NY, USA). The SCMs were filtered with a Laplace filter (high-pass: 50 pixels, 1064 µm) followed by a boxcar filter (low-pass: 5 pixels, 106 µm).

2.7. Data analysis

2.7.1. Cortical electrode recordings

The population signals, MUA and LFP, were simultaneously available at all functioning cortex electrodes (~80%) and good SUA (at ~25% electrodes) were detected after the initial electrode positioning in the upper layers without any search for large spikes. Responses to identical stimulus repetitions were averaged with respect to stimulus onset to obtain peri-stimulus time histograms (PSTHs) from which we determined the cortical response thresholds, delays, and strengths to retinal stimulation. These measures were based on average response power after scaling to the corresponding pre-stimulus values. In addition, LFP and MUA response power were plotted in relation to stimulation strength to estimate thresholds.

2.7.2. Optical recordings of intrinsic cortical signals

The optical recordings of intrinsic signals evoked by electrical retinal stimulation revealed two-dimensional activity patterns in a cortical area of 6 × 8 mm. The grey values of the respective maps coded the activity on a 0–255 gray scale with 0 (black) representing maximal, and 255 (white) minimal activation. The peaks in the spatial pattern of activation were used for estimation of spatial resolution.

Spatial resolution was estimated from the spread of cortical activation in response to a focal retinal stimulus, defined as the retino-cortical point spread function. It was either derived by sampling from linear electrode arrays with 0.3 or 0.5 mm spacing (7 or 16 microelectrodes) or by measuring the spread of activation with optical imaging. For electrode recordings, the spatial distribution of response amplitudes was fitted by a Gaussian function and its full width at half height was taken as the magnitude of the cortical point spread. In addition to this, the same procedure was used to determine the cortical point spread to visual retinal stimulation. In this case, a small focal flash was shown at the same retinal location in the corresponding location of the non-implanted eye (results not shown).

Most response profiles were measured with cortical microelectrode recordings between 4° and 9° retinal eccentricity. The remaining optical recordings were from 0° to 15° eccentricity. To compare these different profiles, we took the magnification factor from the cat visual cortical maps (thoroughly measured by Tusa et al., 1978 & Tusa et al., Tusa, Rosenquist, & Palmer, 1979) at the recording site of every single cortical activation profile. For comparison, we took the individual magnification factors for normalization to a reference eccentricity of 2° visual angle. We chose this reference at 2° because the retina implants in progress will probably span a total visual angle of about ±4°, so that 2° eccentricity is just half way out from the center. The response profiles measured with cortical electrodes were recorded at eccentricities between 4° and 9° in the lower visual field where the magnification factor in cat does not change very much with eccentricity. The fewer optical recordings were made at eccentricities between 0° and 15°. This normalization seems appropriate when we assume that the size of a retinal patch, activated by a single electrode, is independent of eccentricity because the spread of the electrical stimulation field will not change with eccentricity. Therefore the corresponding activation patch in area 17 decreases with increasing eccentricity, and this effect has been normalized by us.

Estimates of resolutions for contrast and time were obtained with two methods. In the "direct approach," the effective duration and variance of averaged excitatory cortical MUA and LFP activations were related to temporal and amplitude resolutions, respectively. The number of discriminable amplitudes was quantified by the difference between average post- and pre-stimulus amplitudes, and divided by the post-stimulus variance. In the "indirect approach," the rate of transinformation T′ (in bit/s) was used (e.g., Eckhorn & Pöpel, 1975; Eger et al., 2005; Shannon, 1948). It determines the amount of information transmitted from a retinal stimulus electrode to a cortical recording site. 1 bit/s here means that two different stimuli can be distinguished by an ideal observer on the basis of a single observation period of 1 s duration. If, for example, 20 bit/s are transmitted from a retinal stimulation electrode to a cortical recording site (a realistic example), a series of twenty 2-level discriminations (e.g., black/white) are safely transmitted during one second (or 5 consecutively transmitted values per second at a resolution of $2^4 = 16$ different levels; e.g., local contrast values, which also gives 5 × 4 bit = 20 bit/s). Hence, temporal and intensity resolutions are inversely correlated, the higher the temporal the lower the intensity resolution. The Shannon information measure has the advantage that the actual noise level is taken into account so that potential resolutions can be estimated quantitatively for single responses without averaging.

3. Results

3.1. Spatial activation profiles in visual cortex

3.1.1. Microelectrode recordings in visual cortex

The cortical responses evoked by single retinal impulses show different time courses (e.g., Figs. 1A, a and b), depending on the recording location relative to the retinal stimulation site. These differences in time course are, in essence, a sign of fast dynamic changes in the spatial activation profiles. We measured the spatial width of these profiles to estimate the potential spatial resolution obtainable with retina implants. The narrowest distribution is generally present at the first afferent cortical activations (Fig. 1A, gray time slices). One millimeter difference in epi-retinal stimulus location causes in this example a cortical offset in the maximal primary response of ~3 mm (Figs. 1A, a vs. b). The later (secondary) response components display a broader distribution.

The spatial activation profiles (retino-cortical point spread) to epi-retinal stimulation have almost equally often a single (Fig. 2A) or a double peak (Fig. 2B). It can also be noticed that the width of the activation increases slightly with stimulation current (Figs. 2A and B), probably due to an increase in the number of recruited ganglion cells and the related broader and stronger activation of the cortex. A coarse estimate of the full width at half height (FWHH) obtained was 1.0 mm (Fig. 2A; stimulation: each phase 0.2 ms, negative first, 24 μA), 2.7 mm (2B; stimulation: each phase 0.2 ms, negative first, 25 μA) and 1.7 mm (2C; stimulation: each phase 0.5 ms, positive first, 50 μA). For a better comparison of these values, obtained at different retinal eccentricities, we normalized these FWHH values to an eccentricity of 2° visual angle by using the cortical magnification factors corresponding to each of our cortical recording locations (Tusa et al., 1978; Tusa et al., 1979). Normalization resulted in 1.4° (A), 3.8° (B), and 2.4° (C) of visual angle, respectively (see also Section 4).

3.1.2. Optical recordings in visual cortex

Optical recordings revealed results that corresponded well to the microelectrode recordings. While the fast response components could not be monitored separately because of the relatively low temporal resolution of the optical signals, the compound signals of optical recordings revealed activation profiles similar to the late components of the microelectrode recordings. This is demonstrated in Fig. 3 showing different cortical activation profiles in response to different single site retinal stimuli (visual stimulation (Fig. 3A), as well as epi- (Fig. 3B), and sub-retinal (Fig. 3C) electrical stimulation). In line with the

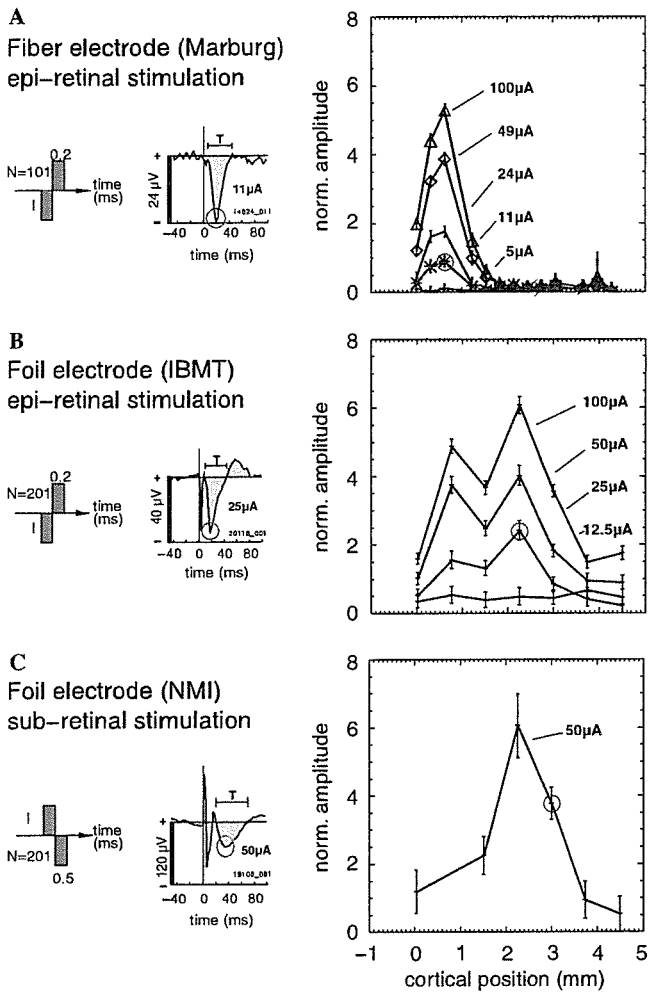

Fig. 2. Spatial cortical activation profiles (right panels) recorded with microelectrodes in response to para-centrally applied single retinal stimulation impulses of different currents I. The normalized amplitudes of the responses for deriving the spatial profiles were taken from the maxima of the first cortical response component after the stimulation artifact (indicated by circles in middle panels, showing example time courses of averaged LFPs at the indicated stimulation currents I; delays of maxima 20–30 ms. T denotes the duration of the first cortical response component). (A) Epi-retinal stimulation with cone electrodes. (B) Epi-retinal stimulation with single electrode of foil array (manufactured by IBMT St. Ingbert, Germany). (C) Sub-retinal stimulation with foil electrode array (manufactured by NMI, Tübingen, Germany). Left panels: time courses of the stimulus current I; number at first impulse indicates its duration in ms, *N* denotes the number of identical stimulus repetitions used for averaging the responses (examples shown in middle panels).

retinotopic organisation of the visual cortex (Tusa et al., 1978, 1979), the cortical activation was localized more posterior when the stimulation was located at lower positions in the retina and moved progressively towards anterior for stimulation sites at upper retinal locations. For a semi-quantitative analysis of the cortical activity, two-dimensional activation profiles were computed on the basis of the gray scale values of the images (Figs. 3B and C). From such data the width of the distributions and their offsets with changes in retinal stimulus location were estimated. A shift of the stimulus by 1.5 mm on the retina led to a shift of the maximum of cortical activation by 3.72 mm (left and rightmost panels in Fig. 3B). The full width at half height (FWHH) of the activity modulation in space was on average 1.78 mm. This FWHH is taken as a measure to estimate the possible spatial resolution (possible discrimination of two adjacent activity profiles) at a given eccentricity along the antero-posterior axis in visual area 18. We have calculated this resolution for the chosen retinal reference eccentricity of 2° (see Section 2: spatial resolution) where 1.78 mm in the visual cortex corresponds to about 2.5° visual angle (Tusa et al., 1979). For these measurements stimulation currents were ±150 µA (250 µs duration of each phase was used for epi-retinal stimuli; s. Fig. 3B) and ±50 µA for the sub-retinal stimuli (1 ms each phase; s. Fig. 3C).

Sub-retinal stimulation and optical recordings revealed similar results as obtained with epi-retinal stimulation. The examples in Fig. 3C show optically recorded activations in response to impulses applied to two different retinal electrodes 0.33 mm apart. They are clearly different in their cortical extent and position of the optical signals. This is demonstrated by the one-dimensional profiles in Fig. 3C. With a 0.33 mm shift of retinal stimulation in the immediate vicinity of the area centralis, the maximum of the cortical signal moves about 1.75 mm on the visual cortical surface. From the 2-D distribution of the activity profiles the spatial extent of activation was measured as FWHH in the same way as for the epi-retinal stimulation. The average value of 1.79 mm FWHH corresponds to approximately 2.5° visual angle at the reference retinal eccentricity of 2° (see Section 2) along the antero-posterior axis in cat visual area 18. This spatial resolution of the optical imaging signal is equivalent to that obtained with epi-retinal stimulation.

Table 1 gives an overview of the estimated spatial resolutions obtained with epi- and sub-retinal stimulation assessed with cortical microelecrode and optical recordings. Resolutions obtained with microelectrode recordings were about a factor of two higher than those with optical recordings. While we measured the highest resolutions (0.68°) with cone-shaped three-dimensional electrodes and epi-retinal stimulation, best results with flat two-dimensional film electrodes (0.9°) were obtained with sub-retinal stimulation.

3.2. Temporal properties of the retino-cortical pathway with electrical activations

Temporal properties of the retino-cortical pathway were analyzed with microelectrode recordings of single and multiple unit spikes (MUA) as well as local field potentials (LFP).

3.2.1. Spike activation patterns of retinal ganglion cells

Spike patterns of microelectrode recordings from the optic tract and retinal stimulation by thin-film arrays were

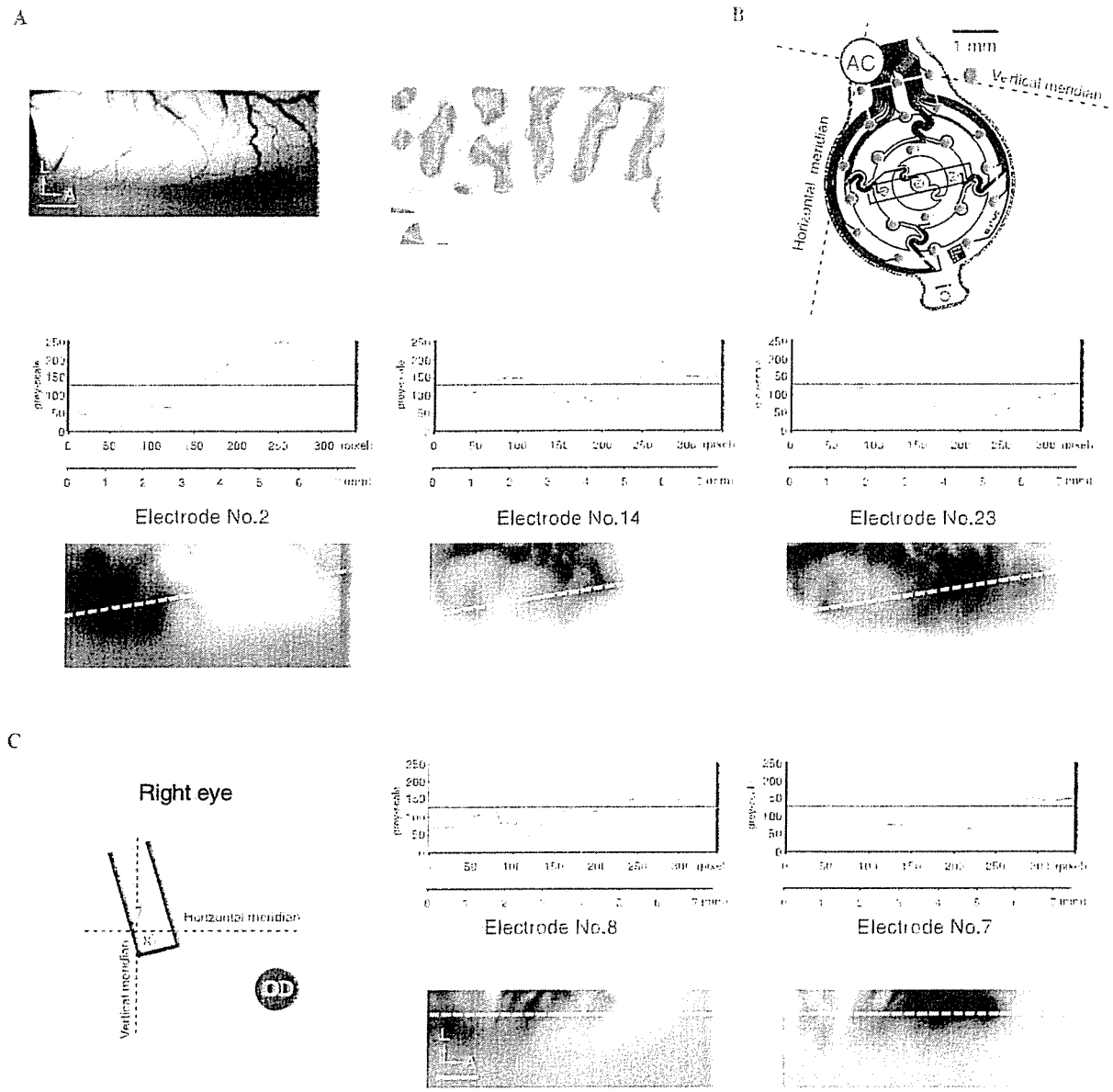

Fig. 3. Optically recorded cortical activations by visual (A), electrical epi- (B), and sub-retinal (C) stimulation with neighboring retinal electrodes. (A) Visual stimulation through a stationary horizontally oriented slit (0,5° width, 40° length) with a moving grating (see Section 2) positioned at vertical retinal eccentricities (elevation) corresponding (from left to right) to the electrode positions 2, 14, 23 in (B). The optical recordings demonstrate the spread and retinotopic displacement of visually evoked cortical activation profiles in cat area 18 (SCMs, see Section 2). (B and C) Optically recorded activation profiles (SCMs) during stimulation with spatially displaced retinal electrodes. Graphs above each optical image show one dimensional activation profiles transformed from the intensity (gray scale) levels along the broken lines (minima represent maximal activation). Considerable cortical activation is represented by the darkest black spots. They move successively from left to right with visual and electrical stimuli and are of similar size with visual and electrocal stimuli. Differences are mainly due to the long slit visual and the focal electrical stimulation. The optical images show responses to stimulation of neighboring electrodes separated by 750 μm (epi-retinal, (B); stimulation current: ±150 μA, 250 μs for each phase) and 330 μm (sub-retinal, (C); stimulation current: ±50 μA, 1 ms for each phase), and reveal activity shifts up to 3,7 mm along the anterior–posterior axis of the cortex (B). Importantly, the cortical magnification factor decreases about exponentially with increasing distance from the projection of the area centralis, and the shifts of the activated cortical locations correspond well to the published retinotopic maps (Tusa et al. 1978; Tusa et al., 1979). The exact position of the stimulation electrodes resulting in the activity images in (B and C) are shown in corresponding insets. Scale bars at optical images 1 mm in (A–C). L, lateral, A, anterior.

analyzed. Fig. 4A shows example montages in which the averaged population responses in the optic tract to single site stimulation are plotted together with the applied current amplitudes. Two important facts are demonstrated here. First, the currents for evoking similar response amplitudes differ by a factor of up to ~20 (from ±4 to ±78 μA;

Table 1
Spatial resolutions obtained with epi- and sub-retinal stimulation

Cortical recording	Epi-retinal stimulation	Sub-retinal stimulation
Optical	2.50° (thin-film electrodes)	2.50° (thin-film electrodes)
Microelectrode array	0.68° (cone electrodes)	
Microelectrode array	1.20° (thin-film electrodes)	0.90° (thin-film electrodes) 1.30° (thin-film electrodes)

The spatial resolution for microelectrode array recordings represents the resolution of the primary response. The lower resolution obtained with optical recordings corresponds well to the spatial resolution of the late responses of microelectrode recordings (see text). The high resolution of 0.68° with epi-retinal stimulation were not obtained with currently available and implantable electrode arrays but with singly in the eye inserted microelectrodes having cone-shaped tips.

epi-retinal stimulation). Second, the response delays (2–3 ms) and their durations (1–2 ms) are very short, indicating that the electrical impulses activate ganglion cells directly and evoke only a single spike per neuron (with epi- and sub-retinal stimulation, Fig. 4A). Fig. 4B shows responses to short light flashes recorded for comparison with the same optic tract electrodes. The composite visually and electrically evoked field responses were observed in a range of 30–200 μV. Compared with the responses to electrical stimuli (delay: 2–3 ms, duration: 1 ms) the visual responses have much longer latencies (~20 ms) and duration (20–35 ms) as is typical for visual population responses in the optic tract to which single ganglion cells generally contribute sequences of several spikes at a broad range of delays and with a higher degree of jitter compared to electrical impulse activation.

3.3. Activation of cortical neurons

3.3.1. Temporal precision of primary cortical action potentials

Retinal electrical stimuli evoked single impulses in ganglion cells with a repetition jitter of <1 ms (Figs. 4 and 5). Because signal transmission across geniculate synapses is highly stable in the applied frequency range of electrical stimulation (Eysel, Grüsser, & Pecci Saavedra, 1974) effective activation volleys will arrive at the primary cortical synapses also with low temporal jitter. Hence, primary cortical spikes can also be generated with high temporal precision. This is demonstrated in Fig. 5. The retino-cortical delay for the first evoked spike in this example is about 6 ms with a jitter <1 ms. For a given cortical recording location, delay and jitter depend on stimulation current and electrode type. The stronger the retinal activation the shorter the latency and the less variable the response. Fig. 5 also shows a pause after the primary spikes of about 2 ms followed by a less precise second spike. We cannot decide on our present data whether the second spikes are due to a primary activation by parvo- or konio-cellular afferents or whether they are secondary spikes in response to magnocellular input (for comparison of these cell types, see: Xu, Ichida, Allison, Bonds, & Casagrande, 2001). In summary, our results show that the visual pathway, from electrical stimulation of retinal ganglion cells to the primary responses in visual cortex, shows a high temporal precision,

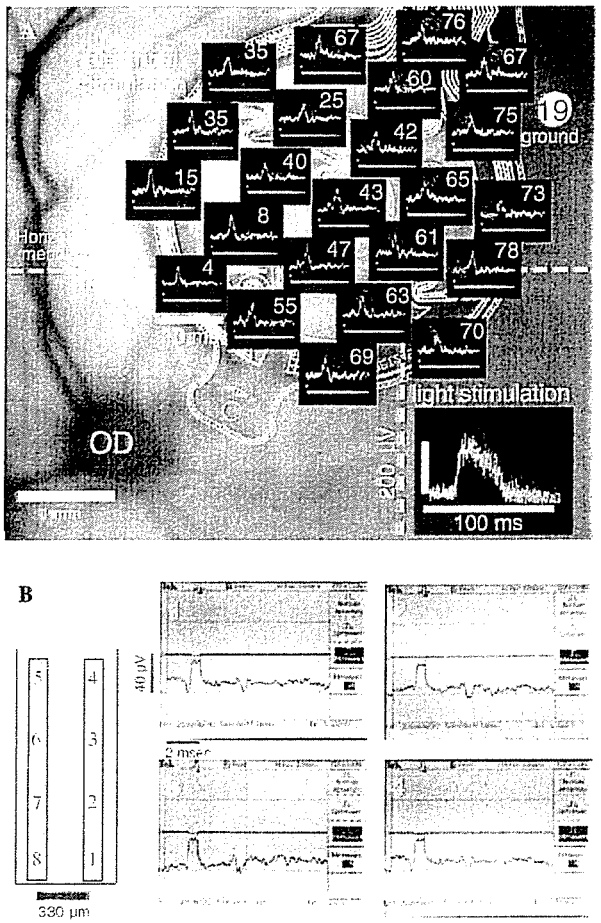

Fig. 4. Epi- and sub-retinal stimulation with thin-film electrodes and population spike recordings from the optic tract. (A) Image of the retinal implant (inter-electrode distance 750 μm) in the upper nasal quadrant of the retina overlapping area centralis. Schematic montage of thin-film array in front of retinal background superimposed by average response waveforms (small insets) evoked by short, single biphasic stimuli (±4 to ±78 μA; balanced current; waveform: 250 μs negative; 250 μs off; 250 μs positive) delivered at 1 Hz via single electrodes of the implant against ground (19). Optic tract recordings were made with a concentric bipolar tungsten electrode (SNEX-100, Rhodes Medical, Woodland Hills, CA, USA). For positioning of the recording electrode and comparison to electrical stimulation, recordings were made during 1 Hz stroboscopic light stimulation (lower right inset). Note the difference in the latency from stimulus onset to the peak responses for optical (about 20 ms) and electrical stimulation (about 2.5 ms). OD: optic disk. (B) Position of the dual in line thin-film array relative to area centralis (case S-R02) is shown to the left. The tip of the array (electrodes 1, 8) covered the foveal zone whereas the other electrodes extended along the vertical meridian in the upper hemi-retina (inter-electrode distance 330 μm). Evoked potentials to electrical stimulation (50 μA, biphasic current pulses, averaged response to 128 identical repetitions) delivered by electrodes 1, 2, 3, and 4, respectively, against the combined electrodes 5–8 of the implant as ground. Please note the slightly longer latency (about 3 ms) after sub-retinal in comparison to epi-retinal electrical stimulation.